SANDIA REPORT
SAND2015-9144
Unlimited Release
Printed May 2015

A Spatial-frequency Method for Analyzing Antenna-to-Probe Interactions in Near-field Antenna Measurements

Billy C. Brock

Prepared by
Sandia National Laboratories
Albuquerque, New Mexico 87185 and Livermore, California 94550

Sandia National Laboratories is a multi-program laboratory managed and operated by Sandia Corporation, a wholly owned subsidiary of Lockheed Martin Corporation, for the U.S. Department of Energy's National Nuclear Security Administration under contract DE-AC04-94AL85000.

Issued by Sandia National Laboratories, operated for the United States Department of Energy by Sandia Corporation.

Available to DOE and DOE contractors from

U.S. Department of Energy
Office of Scientific and Technical Information
P.O. Box 62
Oak Ridge, TN 37831

Telephone: (865) 576-8401
Facsimile: (865) 576-5728
E-Mail: reports@adonis.osti.gov
Online ordering: http://www.osti.gov/bridge

Available to the public from

U.S. Department of Commerce
National Technical Information Service
5285 Port Royal Rd.
Springfield, VA 22161

Telephone: (800) 553-6847
Facsimile: (703) 605-6900
E-Mail: orders@ntis.fedworld.gov
Online order: http://www.ntis.gov/help/ordermethods.asp?loc=7-4-0#online

SAND2015-9144
Unlimited Release
Printed May 2015

A Spatial-frequency Method for Analyzing Antenna-to-Probe Interactions in Near-field Antenna Measurements

Billy C. Brock
bbrock@sandia.gov

RF & Electronic Systems Center
Airborne Intelligence, Surveillance & Reconnaissance (ISR) Systems
ISR Electromagnetics & Sensor Technologies Department
Sandia National Laboratories
P.O. Box 5800
Albuquerque, NM 87185-0533

Abstract

The measurement of the radiation characteristics of an antenna on a near-field range requires that the antenna under test be located very close to the near-field probe. Although the direct coupling is utilized for characterizing the near field, this close proximity also presents the opportunity for significant undesired interactions (for example, reflections) to occur between the antenna and the near-field probe. When uncompensated, these additional interactions will introduce error into the measurement, increasing the uncertainty in the final gain pattern obtained through the near-field-to-far-field transformation. Quantifying this gain-uncertainty contribution requires quantifying the various additional interactions. A method incorporating spatial-frequency analysis is described which allows the dominant interaction contributions to be easily identified and quantified. In addition to identifying the additional antenna-to-probe interactions, the method also allows identification and quantification of interactions with other nearby objects within the measurement room. Because the method is a spatial-frequency method, wide-bandwidth data is not required, and it can be applied even when data is available at only a single temporal frequency. This feature ensures that the method can be applied to narrow-band antennas, where a similar time-domain analysis would not be possible.

Contents

Introduction

Near-field antenna measurement methods are employed to obtain the *far-field* radiation characteristics of an antenna by probing the electromagnetic field very close to the antenna under test, and then applying mathematical transforms to compute the field at a very large distance from the antenna [1, 2, 3]. Because the antenna and the probe are in very close proximity, the desired direct coupling is not the only interaction of significance. Unwanted interactions are also present, and they can have an impact on the accuracy of the measurement. These interactions are manifest by mutual coupling in the form of multiple reflections between the antenna and probe structures, as well as reflections from other objects, and their presence will ultimately lead to uncertainty in the measured antenna gain. A new method is described for detecting and quantifying these interactions, and a conservative estimate of the resulting contribution to the uncertainty in the measured gain is given.

As a starting point, the nature of the near field will be examined. This will provide insight into the behavior of the reflections to be expected with near-field measurements. Next, using this basis, an idealized situation that is amenable to closed-form analytical analysis will be developed to illustrate the spatial-frequency analysis method and its ability to isolate the reflections from the direct coupling. Finally, the method will be applied to actual data measured on the large near-field range at Sandia's Facility for Antenna and Radar-cross-section Measurement (FARM), illustrated in Figure 1.

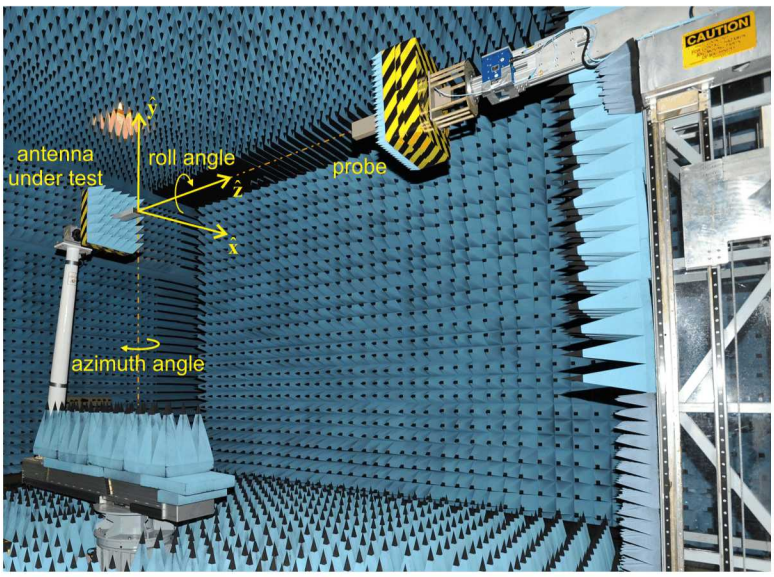

Figure 1 *The large near-field range at the Sandia Facility for Antenna and Radar-cross-section Measurement (FARM), showing the coordinate system associated with a spherical near-field measurement. The probe-to-antenna spacing is variable, and is often much less than shown here.*

Intuition might suggest that time-domain analysis would be very useful in isolating the reflections. Such an analysis requires a short time-domain pulse width, or equivalently a large temporal-frequency bandwidth, to resolve reflections over the short distances involved with near-field measurements. Spatial-frequency analysis, unlike time-domain analysis, does not require a wide bandwidth. In fact, it can even be applied to a measurement at a single frequency. This is particularly fortuitous, since the reflections in a near-field measurement occur over very short distances, requiring extremely wide bandwidths (much wider than supported by many antennas) for the time-domain analysis to be able to resolve them. As a practical matter, this would make the time-domain approach applicable to only a small subset of antennas: those that could support an extraordinary bandwidth. In contrast, the spatial-frequency analysis can be applied to any antenna, regardless of how narrow or wide its supported bandwidth.

As a brief introduction, consider an open-ended waveguide probe and horn antenna aligned along their bore-sight directions and separated by a distance *z*, as illustrated in Figure 2. The coordinate axes used for the analysis is the same as used with near-field measurements at the FARM, and is illustrated in both Figure 1 and Figure 2. In the latter illustration, the direct-coupling path (dark blue) and the path of the first reflection (light blue) are shown. For a specified separation distance z, the length of the propagation path for the direct coupling is simply z, while that of the first reflection is approximately $3z$. As z varies, the spatial frequencies associated with the responses of the two components differ. In the following, exactly how the z-axis spatial-frequency analysis takes advantage of this difference in propagation-path length will be described. First, before examining the details of the method, it will be useful to examine the nature of the near field.

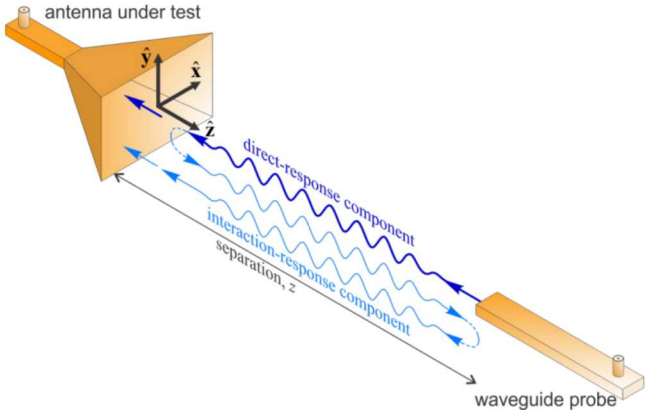

Figure 2 Illustration of the direct path (propagation distance z), and first-order interaction path (propagation distance 3z) between the probe and antenna under test.

The nature of the near field

If the probe is located at a sufficient distance from the antenna, the directly coupled field will be dominated along the bore-sight direction by a spherical-wave component proportional to $|\vec{\mathbf{r}}|^{-1}$. However, near-field measurements often impose spacing of only a few wavelengths, where field terms with other than $|\vec{\mathbf{r}}|^{-1}$ dependence might also be important. Examination of the free-space electric-field dyadic Green's function can provide insight into the need to include terms with $|\vec{\mathbf{r}}|^{-2}$ or even $|\vec{\mathbf{r}}|^{-3}$ dependence when evaluating the uncertainty contribution of multiple reflections between the probe and test antenna.

The free-space electric-field dyadic Green's function for a monochromatic field is a solution of the inhomogeneous vector Helmholtz equation [4]

$$\nabla\times\nabla\times\bar{\bar{\mathbf{G}}}\left(\vec{\mathbf{r}}\,|\,\vec{\mathbf{r}}'\right)-k_0^2\bar{\bar{\mathbf{G}}}\left(\vec{\mathbf{r}}\,|\,\vec{\mathbf{r}}'\right)=\bar{\bar{\mathbf{I}}}\delta\left(\vec{\mathbf{r}}-\vec{\mathbf{r}}'\right), \tag{1}$$

where $\bar{\bar{\mathbf{I}}}=\hat{\mathbf{x}}\hat{\mathbf{x}}+\hat{\mathbf{y}}\hat{\mathbf{y}}+\hat{\mathbf{z}}\hat{\mathbf{z}}=\hat{\mathbf{r}}\hat{\mathbf{r}}+\hat{\boldsymbol{\theta}}\hat{\boldsymbol{\theta}}+\hat{\boldsymbol{\phi}}\hat{\boldsymbol{\phi}}$ is the unit dyad. The $\hat{\mathbf{x}},\hat{\mathbf{y}},\hat{\mathbf{z}}$ unit vectors define the axes in the reference coordinate system, and the $\hat{\mathbf{r}},\hat{\boldsymbol{\theta}},\hat{\boldsymbol{\phi}}$ are the usual spherical unit vectors. The time dependence $e^{+j\omega t}$ will be assumed, where the radian frequency is $\omega=2\pi f$, f is the temporal frequency, $k_0=\omega_0/c$, and c is the speed of light[1].

[1] $c=2.99792458\cdot10^8$ m/s is the *exact* speed of light in the vacuum, and ultimately it is used to define the standard length of the meter. The speed of light in air is slower by about 0.03% to 0.05%, depending on temperature and water-vapor content (see tables for dry air and saturated water vapor in [5]). Using the vacuum value for propagation in air will cause distances derived from the measured delay to be long by about 0.03% to 0.05%. Sometimes using $c\approx3\cdot10^8$ m/s, which is in error from the

The dyadic Green's function is

$$\bar{\bar{\mathbf{G}}}\left(\vec{\mathbf{r}}\middle|\vec{\mathbf{r}}'\right)=\left(\bar{\bar{\mathbf{I}}}+\frac{1}{k_0^2}\nabla\nabla\right)\frac{e^{-jk_0\left|\vec{\mathbf{r}}-\vec{\mathbf{r}}'\right|}}{4\pi\left|\vec{\mathbf{r}}-\vec{\mathbf{r}}'\right|}, \tag{2}$$

where $\vec{\mathbf{r}}$ locates the field point, and $\vec{\mathbf{r}}'$ locates the source point. Since it can be shown that

$$\nabla\nabla\frac{e^{-jk_0\left|\vec{\mathbf{r}}-\vec{\mathbf{r}}'\right|}}{4\pi\left|\vec{\mathbf{r}}-\vec{\mathbf{r}}'\right|}=-\left[\left(\frac{1}{\left|\vec{\mathbf{r}}-\vec{\mathbf{r}}'\right|^2}+j\frac{k_0}{\left|\vec{\mathbf{r}}-\vec{\mathbf{r}}'\right|}\right)\left(\bar{\bar{\mathbf{I}}}-3\frac{\vec{\mathbf{r}}-\vec{\mathbf{r}}'}{\left|\vec{\mathbf{r}}-\vec{\mathbf{r}}'\right|}\frac{\vec{\mathbf{r}}-\vec{\mathbf{r}}'}{\left|\vec{\mathbf{r}}-\vec{\mathbf{r}}'\right|}\right)+\frac{\vec{\mathbf{r}}-\vec{\mathbf{r}}'}{\left|\vec{\mathbf{r}}-\vec{\mathbf{r}}'\right|}\frac{\vec{\mathbf{r}}-\vec{\mathbf{r}}'}{\left|\vec{\mathbf{r}}-\vec{\mathbf{r}}'\right|}\right]\frac{e^{-jk_0\left|\vec{\mathbf{r}}-\vec{\mathbf{r}}'\right|}}{4\pi\left|\vec{\mathbf{r}}-\vec{\mathbf{r}}'\right|}, \tag{3}$$

the free-space dyadic Green's function can be expanded as

$$\bar{\bar{\mathbf{G}}}\left(\vec{\mathbf{r}}\middle|\vec{\mathbf{r}}'\right)=\left[\bar{\bar{\mathbf{I}}}-\frac{\left(\vec{\mathbf{r}}-\vec{\mathbf{r}}'\right)}{\left|\vec{\mathbf{r}}-\vec{\mathbf{r}}'\right|}\frac{\left(\vec{\mathbf{r}}-\vec{\mathbf{r}}'\right)}{\left|\vec{\mathbf{r}}-\vec{\mathbf{r}}'\right|}-\left(j\frac{1}{k_0\left|\vec{\mathbf{r}}-\vec{\mathbf{r}}'\right|}+\frac{1}{k_0^2\left|\vec{\mathbf{r}}-\vec{\mathbf{r}}'\right|^2}\right)\left(\bar{\bar{\mathbf{I}}}-3\frac{\left(\vec{\mathbf{r}}-\vec{\mathbf{r}}'\right)}{\left|\vec{\mathbf{r}}-\vec{\mathbf{r}}'\right|}\frac{\left(\vec{\mathbf{r}}-\vec{\mathbf{r}}'\right)}{\left|\vec{\mathbf{r}}-\vec{\mathbf{r}}'\right|}\right)\right]\frac{e^{-jk_0\left|\vec{\mathbf{r}}-\vec{\mathbf{r}}'\right|}}{4\pi\left|\vec{\mathbf{r}}-\vec{\mathbf{r}}'\right|}. \tag{4}$$

For a specified source current-density distribution, $\vec{\mathbf{J}}\left(\vec{\mathbf{r}}'\right)$, the electric field outside the source region, at position $\vec{\mathbf{r}}$, is obtained by integrating the dot product of the source current-density vector against the dyadic Green's function over the volume, V, containing the source current, [4]

$$\vec{\mathbf{E}}\left(\vec{\mathbf{r}}\right)=-j\omega\mu_0\int_V\vec{\mathbf{J}}\left(\vec{\mathbf{r}}'\right)\cdot\bar{\bar{\mathbf{G}}}\left(\vec{\mathbf{r}}\middle|\vec{\mathbf{r}}'\right)dV'. \tag{5}$$

Examination of (4) shows the integrand of (5) will contain components that vary with inverse powers of the distance from the source point to the field point, but only first, second, and third inverse powers are present. Also, the second and third inverse powers are associated with all directions of source and field vectors, while the first inverse power is associated only with vector components of the field that are orthogonal to the direction pointing directly from the source point to the field point. In particular, vector components of the source that point directly from the source point to the field point can only contribute to the second and third inverse power terms, and only to vector components of the electric field that are parallel to this line of sight.

Without knowing any details of the current distribution producing the electric field, precise estimates of the relative importance of the various terms is difficult. However, consider the series expansion

$$\frac{1}{k_0^{n-1}\left|\vec{\mathbf{r}}-\vec{\mathbf{r}}'\right|^n}=\frac{1}{k_0^{n-1}r^n}\begin{pmatrix}1+n\cos(\psi)\dfrac{r'}{r}+\dfrac{n}{2}\left((n+2)\cos^2(\psi)-1\right)\dfrac{r'^2}{r^2}+\\ \dfrac{n(n+2)}{6}\cos(\psi)\left((n+4)\cos^2(\psi)-3\right)\dfrac{r'^3}{r^3}+\\ \dfrac{n(n+2)}{24}\left((n+4)\cos^2(\psi)\left((n+6)\cos^2(\psi)-6\right)+3\right)\dfrac{r'^4}{r^4}+\cdots\end{pmatrix},\ n\in\{1,2,3\}, \tag{6}$$

where $\cos\left(\psi\right)=\hat{\mathbf{r}}\cdot\hat{\mathbf{r}}'$, $r=\left|\vec{\mathbf{r}}\right|$, and $r'=\left|\vec{\mathbf{r}}'\right|$. After substitution of (6) into (4) and forming the dot product with the source current-density vector, the result of the integration over $\vec{\mathbf{r}}'$ in (5) will be three integrals, each proportional to r^{-1}, $k_0^{-1}r^{-2}$, or $k_0^{-2}r^{-3}$, respectively. Each of the integrands will be a vector in r' multiplied by a series in r'/r. The details of $\vec{\mathbf{J}}\left(\vec{\mathbf{r}}'\right)$ will determine how the series resulting from each of the integrals behaves, but estimating the relative size of the terms proportional to $k_0^{1-n}\left|\vec{\mathbf{r}}-\vec{\mathbf{r}}'\right|^{-n}$ in the Green's function gives a rough estimate of the relative importance of the $\left|\vec{\mathbf{r}}\right|^{-n}$ terms in the near-field region for $n=1,2,3$. At a separation of about 16 wavelengths, the second-order term will be about 40 dB

---

vacuum value by less than 0.07%, is appropriate and sufficiently accurate. Distances in vacuum derived from the measured delay with this approximation will be long by about 0.07%. Distances in air will be long by about 0.1% to 0.12%.

below the first-order term. The third-order term will reach 40 dB below the first-order term at a separation of only1.6 wavelengths. Thus, in the realm of near-field measurements, at least the second-order term has a potential to provide a contribution on the order of 0.1 dB or more, depending on the separation. It is clear that a method of analyzing the contribution from the antenna-to-probe interactions should not arbitrarily be limited to only terms with $|\vec{\mathbf{r}}|^{-1}$ dependence. The z-axis spatial-frequency analysis described below does not discriminate between the terms.

Identifying the reflections between the probe and antenna

The reflections between the probe and the antenna under test can be detected by examining measurements of the probe-to-antenna coupling along the bore-sight direction $\hat{\mathbf{r}} = \hat{\mathbf{z}}$ as the separation z is varied (see Figure 2), while looking for response components with phase variation proportional to about $z, 3z, 5z, 7z, \cdots$. The first of these is the desired direct coupling, while the rest identify the first and higher-order reflections between the probe and antenna. In many cases only the first reflection will be significant, but the spatial-frequency analysis described below can detect, identify, and quantify contributions from higher-order reflections, as well as contributions from the walls, floor, and ceiling.

It should again be acknowledged that identifying the phase behavior of the various interaction terms could be accomplished by examining the data either in the temporal-frequency domain or in the spatial domain. Separation and identification of the components requires either the application of an inverse Fourier transform in the frequency domain followed by sorting the resulting time-domain responses according to delay, or the application of a forward Fourier transform in the spatial domain followed by sorting the resulting spatial-frequency responses. However, as already stated, because of the small distances involved, the frequency-domain analysis will require a very wide bandwidth, making that approach unattractive at best or completely useless when the antenna cannot support sufficient bandwidth. Consequently, the time-domain method will not be considered further.

Because many antennas can be narrow-bandwidth designs, collecting data at only a single or a few frequencies while varying the separation distance and subsequently performing a spatial-frequency analysis is a practical approach. The process of computing the spatial frequencies and their interpretation will be described next.

The spatial-frequency analysis of the probe-to-antenna interaction

The relationship between the spatial domain and the spatial-frequency domain is entirely analogous to the relationship between the time domain and the temporal-frequency domain, which may be more familiar and intuitive. An understanding of the spatial-frequency analysis will be facilitated by referring to the arrangement of the antenna under test and field probe illustrated in Figure 2. An analytic model, based on a simplified antenna source, will be derived. Although the specific analytical analysis is for a special, simplified situation, it does apply in principle to the generic case, and the analytic model will allow the spatial-frequency analysis to be examined in a precise manner, without the complication and confusion that might be introduced by a more generalized situation. After the analysis is complete, the method will be applied to measured data using numerical methods, demonstrating remarkable agreement with the analytic model.

For the required simplicity, allow the antenna to be represented by a point current source at the origin,

$$\vec{\mathbf{J}}_{AUT}(\vec{\mathbf{r}}') = \frac{C}{j\omega\mu_0}\delta(\vec{\mathbf{r}}')\hat{\mathbf{y}} \,. \tag{7}$$

From (5), the electric field at $\vec{\mathbf{r}}$ from this simple current source is given by

$$\vec{\mathbf{E}}(\vec{\mathbf{r}}) = -j\omega\mu_0 \iiint_{AUT} \bar{\bar{\mathbf{G}}}(\vec{\mathbf{r}}|\vec{\mathbf{r}}') \cdot \vec{\mathbf{J}}_{AUT}(\vec{\mathbf{r}}')\, d^3\vec{\mathbf{r}}' \,. \tag{8}$$

Using (4) and (7) in (8) and performing the integration gives the electric field radiated from the antenna,

$$\vec{\mathbf{E}}(\vec{\mathbf{r}}) = C\left[\bar{\bar{\mathbf{I}}} - \hat{\mathbf{r}}\hat{\mathbf{r}} - \left(j\frac{1}{k_0 r} + \frac{1}{k_0^2 r^2}\right)\left(\bar{\bar{\mathbf{I}}} - 3\hat{\mathbf{r}}\hat{\mathbf{r}}\right)\right]\cdot\hat{\mathbf{y}}\frac{e^{-jk_0 r}}{4\pi r}. \tag{9}$$

The electric field has components with r^{-1}, r^{-2}, and r^{-3} dependence.

Now, suppose this field is probed by an ideal probe antenna, polarized with the electric field along $\hat{\mathbf{y}}$, and located at $\vec{\mathbf{r}} = z\hat{\mathbf{z}}$. The configuration in Figure 2 will support reflections from the probe, the antenna under test, and their associated supporting structures (not shown). Assuming, again for simplicity, that the reflected fields occur at the apertures of the antenna and probe as illustrated in Figure 2, the voltage measured by the probe as a function of separation distance, z, is

$$v(z) = C'\sum_{n=0}^{\infty}\Gamma_{probe}^{n}\Gamma_{AUT}^{n}\left(1 - j\frac{1}{k_0(2n+1)z} - \frac{1}{k_0^2(2n+1)^2 z^2}\right)\frac{e^{-jk_0(2n+1)z}}{4\pi(2n+1)z}, \tag{10}$$

where n indicates the order of the reflection ($n = 0$ is the direct coupling term), C' includes the probe gain as well as the source strength, and Γ_{probe} and Γ_{AUT} are the complex reflection coefficients at the apertures of the probe and antenna under test, respectively. It is assumed that the probe and horn are terminated in matched impedances at their respective terminals. Other reflections might also be present, and will be addressed subsequently. The voltage in (10) is the spatial-domain response along the z axis.

Information about the spatial frequencies contained in (10) can be obtained by computing the Fourier integral over a finite range of positions along the $\hat{\mathbf{z}}$ axis, $z_{min} \le z \le z_{max}$, giving the spatial-frequency response,

$$V(z_{min}, z_{max}, k) = \int_{z_{min}}^{z_{max}} v(z)e^{jkz}dz = C'\sum_{n=0}^{\infty}\Gamma_{probe}^{n}\Gamma_{AUT}^{n}\frac{1}{4\pi(2n+1)}\left(\begin{array}{l}\displaystyle\int_{z_{min}}^{z_{max}}\frac{e^{-jk_0(2n+1)z}}{z}e^{jkz}dz \\ \displaystyle -j\frac{1}{k_0(2n+1)}\int_{z_{min}}^{z_{max}}\frac{e^{-jk_0(2n+1)z}}{z^2}e^{jkz}dz \\ \displaystyle -\frac{1}{k_0^2(2n+1)^2}\int_{z_{min}}^{z_{max}}\frac{e^{-jk_0(2n+1)z}}{z^3}e^{jkz}dz\end{array}\right). \tag{11}$$

Analogous to the temporal frequency, the spatial frequency is defined from the spatial radian frequency (the wavenumber), k, as

$$f_{spatial} = \frac{k}{2\pi}. \tag{12}$$

The wavenumber, k, is the Fourier transform variable in (11). The spatial frequency associated with the direct coupling is

$$f_0 = \frac{k_0}{2\pi}, \tag{13}$$

and it will become apparent that the spatial frequency associated with the n^{th} reflection is

$$f_n = (2n+1)\frac{k_0}{2\pi}. \tag{14}$$

The relative response at these spatial frequencies can be easily obtained after evaluating the Fourier transform in (11), allowing determination of the strength of the reflection, and therefore the determination of the contribution to measurement uncertainty associated with the individual reflections.

Continuing with the analytic model, the first integral in (11) can be written in terms of sine and cosine integrals,

$$I_1\left(z_{min}, z_{max}, \Delta k_n\right) = \int_{z_{min}}^{z_{max}} \frac{e^{-jk_0(2n+1)z}}{z} e^{jkz}\, dz = \int_{z_{min}}^{z_{max}} \frac{e^{-j\Delta k_n z}}{z} dz$$
$$= \left(ci\left(\Delta k_n\, z_{max}\right) - ci\left(\Delta k_n\, z_{min}\right) - j\left[si\left(\Delta k_n\, z_{max}\right) - si\left(\Delta k_n\, z_{min}\right)\right]\right), \tag{15}$$

where $\Delta k_n = (2n+1)k_0 - k$, and the sine and cosine integrals, as defined in 8.23 in Gradshteyn & Ryzhik [6] for real argument x, are

$$si(x) = -\int_x^\infty \frac{\sin t}{t} dt, \tag{16}$$

and

$$ci(x) = -\int_x^\infty \frac{\cos t}{t} dt. \tag{17}$$

These sine and cosine integrals are plotted in Figure 3.

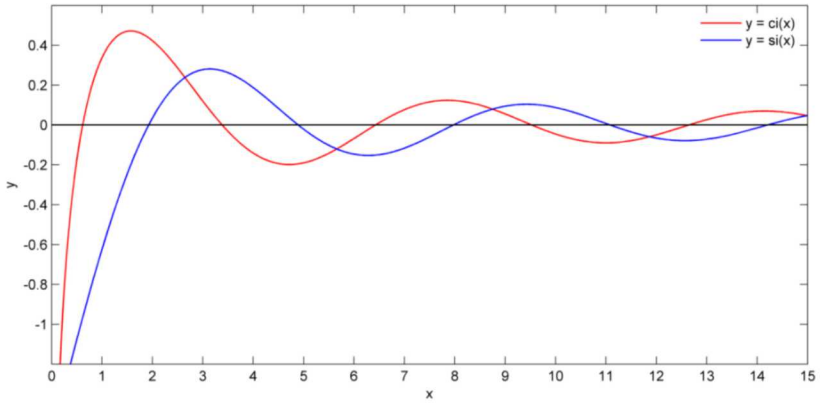

Figure 3 *The sine and cosine integrals,* $si(x) = -\int_x^\infty \frac{\sin t}{t} dt$ *and* $ci(x) = -\int_x^\infty \frac{\cos t}{t} dt$.

Other sine and cosine integrals are also commonly defined (see, for example, 5.2 in Abramowitz & Stegun [7] or the software documentation for *Mathematica* [11]),

$$Si(x) = si(x) + \frac{\pi}{2}, \tag{18}$$

where

$$Si(x) = \int_0^x \frac{\sin t}{t} dt, \tag{19}$$

and

$$Ci(x) = ci(x), \tag{20}$$

where

$$Ci(x) = \gamma + \ln x + \int_0^x \frac{\cos t - 1}{t} dt, \tag{21}$$

and $\gamma = 0.57721566490153286060606512090\cdots$ is Euler's constant[2].

[2] Euler's constant, γ, is one of those fascinating and mysterious mathematical constants that appear in numerous contexts. It has yet to be proven to be irrational [8], although it appears that it might be, and it might even be a transcendental number, but that also has not been proven. Euler's

The integral $I_1\left(z_{min}, z_{max}, \Delta k_n\right)$ is plotted in Figure 4 for $z_{min}=1,\ z_{max}=2$, showing a well-defined peak at $\Delta k_n = 0$. The remaining two integrals are obtained by applying the integration-by-parts procedure,

$$\begin{aligned}\int_{z_{min}}^{z_{max}} \frac{e^{-j\Delta k_n z}}{z^2} dz &= -\frac{e^{-j\Delta k_n z}}{z}\bigg|_{z_{min}}^{z_{max}} - j\Delta k \int_{z_{min}}^{z_{max}} \frac{e^{-j\Delta k_n z}}{z} dz \\ &= \frac{e^{-j\Delta k_n z_{min}}}{z_{min}} - \frac{e^{-j\Delta k_n z_{max}}}{z_{max}} - j\Delta k I_1\left(z_{min}, z_{max}, \Delta k_n\right),\end{aligned} \tag{22}$$

and

$$\begin{aligned}\int_{z_{min}}^{z_{max}} \frac{e^{-jk_0(2n+1)z}}{z^3} e^{jkz} dz &= -\frac{e^{-j\Delta k_n z}}{2z^2}\bigg|_{z_{min}}^{z_{max}} - j\Delta k \frac{1}{2} \int_{z_{min}}^{z_{max}} \frac{e^{-j\Delta k_n z}}{z^2} dz \\ &= \frac{e^{-j\Delta k_n z_{min}}}{2z_{min}^2}\left(1 - j\Delta k_n z_{min}\right) - \frac{e^{-j\Delta k_n z_{max}}}{2z_{max}^2}\left(1 - j\Delta k_n z_{max}\right) - \frac{\Delta k_n^2}{2} I_1\left(z_{min}, z_{max}, \Delta k_n\right).\end{aligned} \tag{23}$$

Thus, the complete response as a function of spatial wavenumber, k, is

$$V\left(z_{min}, z_{max}, k\right) = \sum_{n=0}^{\infty} V_n\left(z_{min}, z_{max}, k\right) \tag{24}$$

where

$$V_n\left(z_{min}, z_{max}, k\right) = C' \Gamma_{probe}^n \Gamma_{AUT}^n \frac{1}{4\pi(2n+1)} \left(\begin{array}{l} \left(1 - \dfrac{\Delta k_n}{k_0(2n+1)} + \dfrac{\Delta k_n^2}{2k_0^2(2n+1)^2}\right) I_1\left(z_{min}, z_{max}, \Delta k_n\right) \\ -j \dfrac{1}{k_0(2n+1)} \left(\dfrac{e^{-j\Delta k_n z_{min}}}{z_{min}} - \dfrac{e^{-j\Delta k_n z_{max}}}{z_{max}} \right) \\ -\dfrac{1}{2k_0^2(2n+1)^2} \left(\dfrac{e^{-j\Delta k_n z_{min}}}{z_{min}^2}\left(1 - j\Delta k_n z_{min}\right) - \dfrac{e^{-j\Delta k_n z_{max}}}{z_{max}^2}\left(1 - j\Delta k_n z_{max}\right) \right) \end{array} \right). \tag{25}$$

The peak spatial-frequency responses occur when $\Delta k_n = 0$, so that

$$k = k_0(2n+1), \tag{26}$$

---

definition, $\gamma = \lim_{m\to\infty} H_m - \ln m$ (see 6.1.3 in Abramowitz and Stegun [7]), where $H_m = \sum_{k=1}^{m} \frac{1}{k}$ is the harmonic number [9], is quite slow to converge and cannot be recommended for computing γ. For example, the magnitude of the error with $m = 1{,}000{,}000$ is about 5×10^{-7}, and with $m = 1{,}000{,}000{,}000$ is about 5×10^{-10}. A better approximation is $\gamma_m = H_m - \ln m - 1/2m$, where $\gamma = \lim_{m\to\infty} \gamma_m$, for which the magnitude of the error is orders of magnitude smaller, being less than 10^{-7} with $m = 1{,}000$ and less than 10^{-13} with $m = 1{,}000{,}000$. A number of even more efficient algorithms have been developed to compute γ [8, 10]. One of these, $\gamma_m = H_m - \ln\left(m + 1/2 + 1/24m\right)$, is accurate to within about 2×10^{-11} with $m = 1{,}000$ and 2×10^{-16} with $m = 50{,}000$. Using the built-in capability of *Mathematica* [11] or *Sage* [12] to compute large numbers of digits of γ, and counting digits to the right of the decimal point, the $3{,}423^{rd}$ through $3{,}427^{th}$ digits are all zero, but this string of 5 zeros gives only fleeting hope that the sequence has terminated and that γ is rational; the sequence of nonzero digits continues on beyond. The sequence of 5 zeros never occurs again in the next 100,000 digits, but it occurs 10 times in the first 1,000,000 digits, and one of these is part of a sequence of 6 consecutive zeros. In fact, sequences containing 5 or more consecutive copies of each of the digits 0 through 9 occur 10, 8, 11, 8, 8, 9, 8, 4, 7, and 14 times, respectively, in the first 1,000,000 digits. Counting all sequences that begin at distinct positions, but which may overlap, the sequences of 5 consecutive copies of the digits 0 through 9 occur 11, 9, 11, 9, 9, 10, 9, 6, 8, and 15 times, respectively, an average of 9.7 times. If the digits are uniformly distributed, the expected number of times each of these sequences should occur is 10. This and other similar tests are consistent with the digits being uniformly distributed, but do not constitute proof. Additional information about Euler's γ can be found in [13, 14].

and the peak of the response due to the n^{th} reflection is

$$V_n\left(z_{min},z_{max},k_0(2n+1)\right)=C'\frac{\Gamma_{probe}^n\Gamma_{AUT}^n}{4\pi(2n+1)}\left(\ln\left(\frac{z_{max}}{z_{min}}\right)-\frac{1}{k_0(2n+1)}\left(\frac{z_{max}-z_{min}}{z_{min}z_{max}}\right)\left(j+\frac{1}{2k_0(2n+1)}\left(\frac{z_{max}+z_{min}}{z_{min}z_{max}}\right)\right)\right). \tag{27}$$

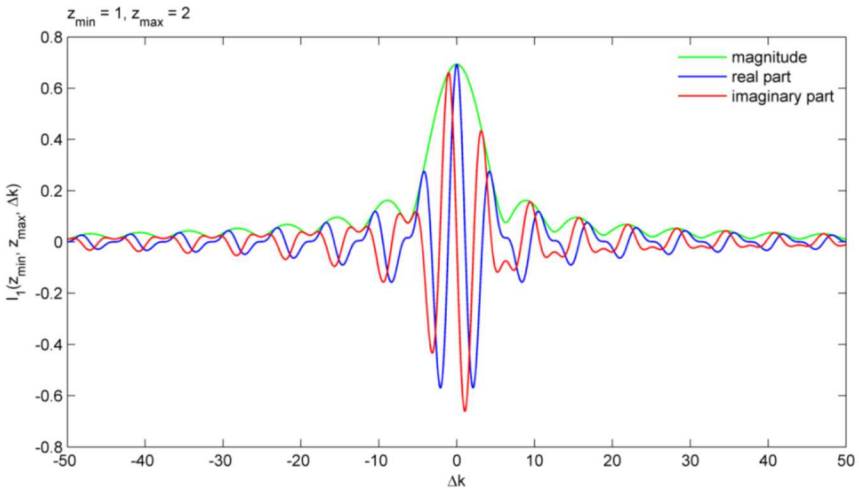

Figure 4 The integral $I_1\left(z_{min},z_{max},\Delta k\right)=\int_{z_{min}}^{z_{max}}\frac{e^{-j\Delta k\,z}}{z}dz$ for $z_{min}=1$ and $z_{max}=2$, as a function of Δk.

The ratio of the peak contribution of the first reflection to the peak contribution of the direct response is

$$\Delta_1=\frac{V_1\left(z_{min},z_{max},k=3k_0\right)}{V_0\left(z_{min},z_{max},k=k_0\right)}=\frac{1}{3}\Gamma_{probe}\Gamma_{AUT}\frac{\ln\left(\frac{z_{max}}{z_{min}}\right)-\frac{1}{3k_0}\left(\frac{z_{max}-z_{min}}{z_{min}z_{max}}\right)\left(j+\frac{1}{6k_0}\left(\frac{z_{max}+z_{min}}{z_{min}z_{max}}\right)\right)}{\ln\left(\frac{z_{max}}{z_{min}}\right)-\frac{1}{k_0}\left(\frac{z_{max}-z_{min}}{z_{min}z_{max}}\right)\left(j+\frac{1}{2k_0}\left(\frac{z_{max}+z_{min}}{z_{min}z_{max}}\right)\right)}. \tag{28}$$

Note that the factor of $1/3$ is the result of the reflected field propagating three times as far. Letting $z_{max}=\alpha z_{min}$, the ratio can be written in the convenient form

$$\Delta_1=\frac{1}{3}\Gamma_{probe}\Gamma_{AUT}\frac{\ln(\alpha)-\frac{1}{6\pi}\frac{\lambda_0}{z_{min}}\frac{\alpha-1}{\alpha}\left(j+\frac{1}{12\pi}\frac{\lambda_0}{z_{min}}\frac{\alpha+1}{\alpha}\right)}{\ln(\alpha)-\frac{1}{2\pi}\frac{\lambda_0}{z_{min}}\frac{\alpha-1}{\alpha}\left(j+\frac{1}{4\pi}\frac{\lambda_0}{z_{min}}\frac{\alpha+1}{\alpha}\right)}. \tag{29}$$

Since $z_{max}>z_{min}$, α is constrained so that $1<\alpha<\infty$. The magnitude of the ratio $\frac{\Delta_1}{\Gamma_{probe}\Gamma_{AUT}}$ is plotted in Figure 5 for $1<\alpha\le 100$ and several values of z_{min}/λ_0. This ratio appears to be nearly independent of both α and z_{min}. The following limits are useful in understanding the behavior of the magnitude:

$$\lim_{\alpha\to 1}\left(\frac{|\Delta_1|}{|\Gamma_{probe}||\Gamma_{AUT}|}\right)=\frac{1}{3}\frac{\sqrt{1-\frac{1}{(6\pi)^2}\frac{\lambda_0^2}{z_{min}^2}\left(1-\frac{1}{(6\pi)^2}\frac{\lambda_0^2}{z_{min}^2}\right)}}{\sqrt{1-\frac{1}{(2\pi)^2}\frac{\lambda_0^2}{z_{min}^2}\left(1-\frac{1}{(2\pi)^2}\frac{\lambda_0^2}{z_{min}^2}\right)}} \qquad \lim_{\alpha\to\infty}\left(\frac{|\Delta_1|}{|\Gamma_{probe}||\Gamma_{AUT}|}\right)=\frac{1}{3}. \tag{30}$$

As $\alpha\to 1$, the ratio approaches a small, finite value, and when α becomes very large, it approaches the simple fraction $1/3$. As can been seen in Figure 5, the value never varies far from $1/3$ when $z_{min}\ge\lambda_0/2$. However, when $z_{min}<\lambda_0/2$, the behavior becomes a little more interesting. For a fixed value of α, as

z_{min} is reduced below about $\lambda_0/3$, the ratio begins to increase slightly, reaches a maximum, and then falls to

$$\lim_{z_{min}\to 0}\left(\frac{\Delta_1}{\Gamma_{probe}\Gamma_{AUT}}\right)=\frac{1}{27}.$$

This behavior is visible in Figure 6, where the magnitude of $\frac{\Delta_1}{\Gamma_{probe}\Gamma_{AUT}}$ is plotted as a function of both z_{min} and α. The maximum is located at

$$z_{min}=\frac{\lambda_0}{3\sqrt{2}\,\pi}\frac{(\alpha+1)}{\alpha}\sqrt{\frac{(\alpha-1)}{(\alpha+1)\ln(\alpha)-(\alpha-1)}\left(\frac{5}{4}+\sqrt{\left(1+\frac{3}{2}\frac{(\alpha-1)}{(\alpha+1)\ln(\alpha)}\right)\left(1-\frac{3}{8}\frac{(\alpha-1)}{(\alpha+1)\ln(\alpha)}\right)}\right)}, \qquad (31)$$

and its value increases slowly as α increases. The maximum of $\frac{|\Delta_1|}{|\Gamma_{probe}||\Gamma_{AUT}|}$ and the value of z_{min} where it occurs are both plotted in Figure 7 as a function of α.

Since the antenna model used here is a point-source current, the propagating field expands spherically. However, for a large distributed antenna, the amplitude dependence on distance might be somewhat different in the near-field region.[3] Nevertheless, the conclusion is that the magnitude of the ratio of the peak of the reflection response to that of the direct response is nearly independent of the parameters of the measurement, and thus gives a reliable indication of the magnitude of the interference from the antenna-to-probe interaction.

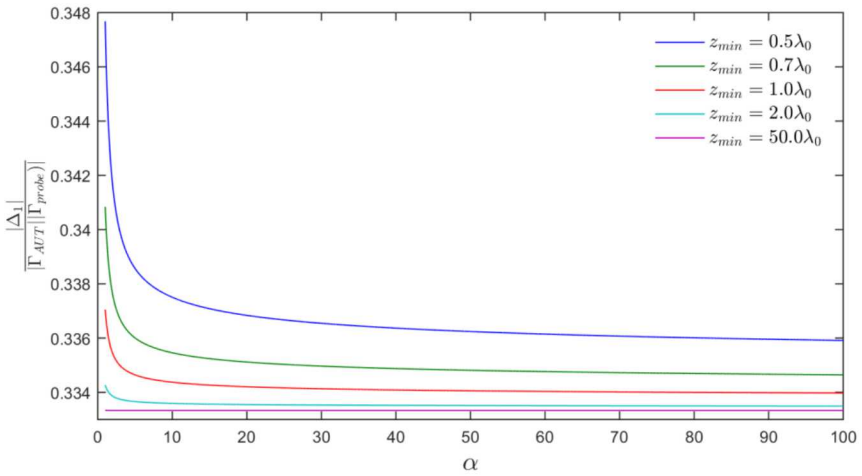

Figure 5 Plot of the magnitude of the ratio $\frac{\Delta_1}{\Gamma_{AUT}\Gamma_{probe}}$ *as a function of* $\alpha>1$ *for several values of* z_{min}.

[3] For example, the field in the very near vicinity of a large planar antenna can behave as a plane wave, while for a well-designed probe, the reflection will exhibit nearly spherical expansion.

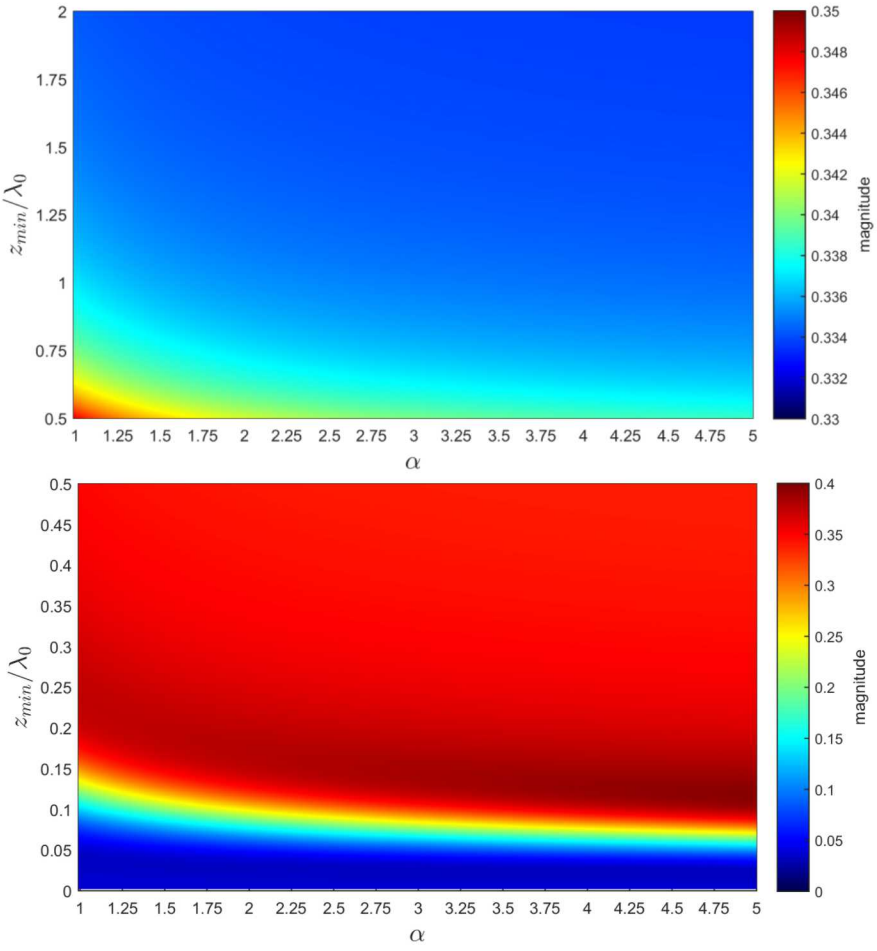

Figure 6 *Plot of the magnitude of the ratio* $\frac{\Delta_1}{\Gamma_{AUT}\Gamma_{probe}}$ *as a function of* $\alpha > 1$ *with* $0 < z_{min}/\lambda_0 \le 0.5$ *(bottom) and* $0.5 \le z_{min}/\lambda_0 \le 2$ *(top). The two plots use different color scales for the magnitude values.*

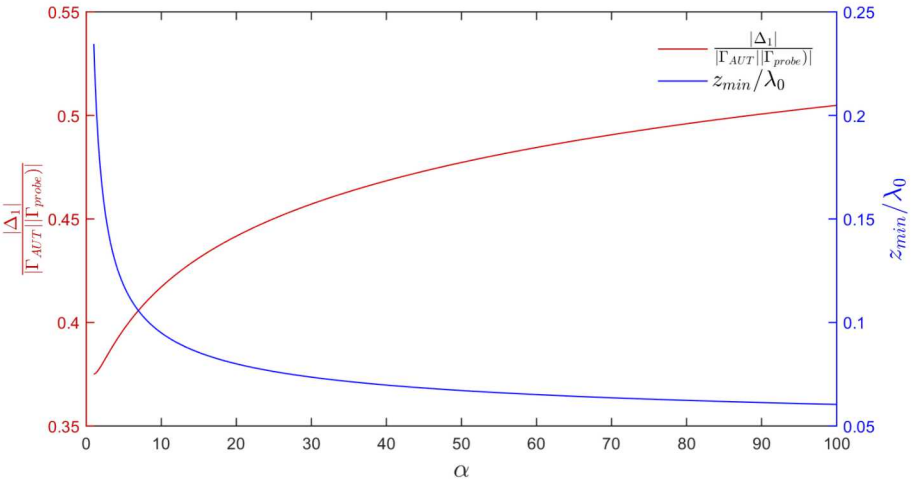

Figure 7 *The value of the peak of* $\frac{\Delta_1}{\Gamma_{AUT}\Gamma_{probe}}$ *(red) and the value of* z_{min}/λ_0 *at which it occurs (blue).*

The phase of Δ_1 is

$$\arg\left(\Delta_1\right)=\arg\left(\Gamma_{probe}\right)+\arg\left(\Gamma_{AUT}\right)+\arg\left(\frac{\ln\left(\alpha\right)-\frac{1}{6\pi}\frac{\lambda}{z_{min}}\frac{\alpha-1}{\alpha}\left(j+\frac{1}{12\pi}\frac{\lambda}{z_{min}}\frac{\alpha+1}{\alpha}\right)}{\ln\left(\alpha\right)-\frac{1}{2\pi}\frac{\lambda}{z_{min}}\frac{\alpha-1}{\alpha}\left(j+\frac{1}{4\pi}\frac{\lambda}{z_{min}}\frac{\alpha+1}{\alpha}\right)}\right). \tag{32}$$

The contribution to the phase from the measurement parameters is negligible for practical values of z_{min}, as seen in Figure 8. Thus, the phase of the ratio is essentially determined by the phase of the reflection coefficients when $z_{min}>\lambda/2$.

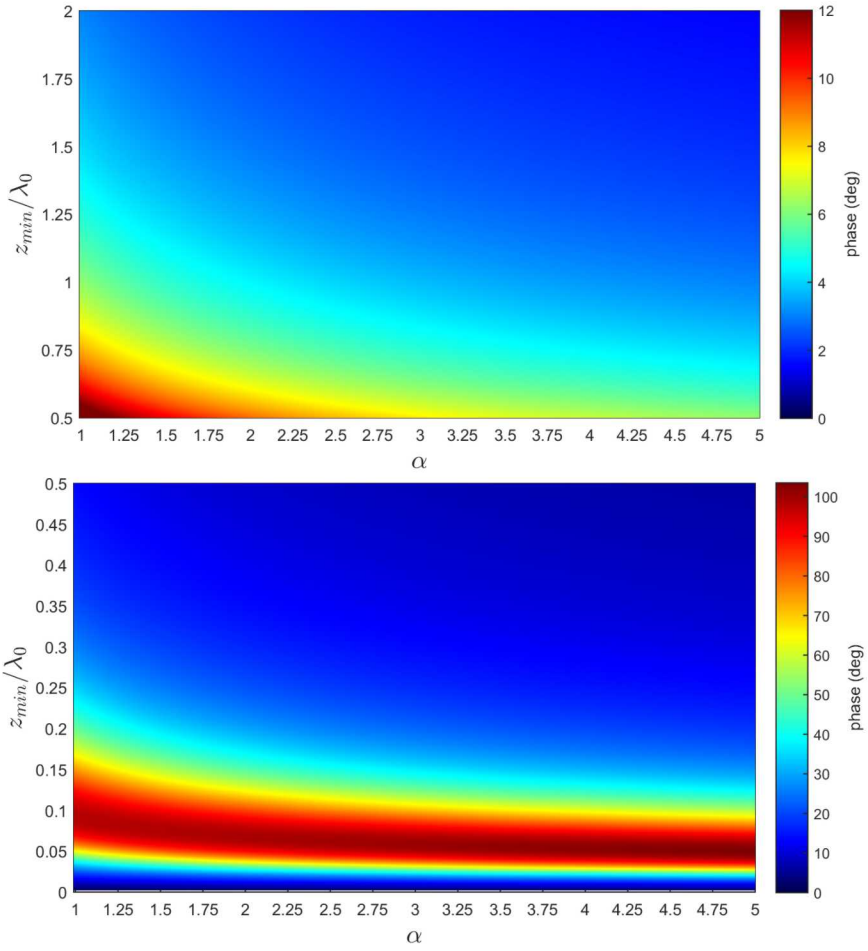

Figure 8 *Phase of* $\frac{\Delta_1}{\Gamma_{probe}\Gamma_{AUT}}$ *for* $1\le\alpha\le5$ *with* $0<z_{min}/\lambda_0\le0.5$ *(bottom) and* $0.5\le z_{min}/\lambda_0\le2$ *(top). Note the different color scales for the phase values.*

Statistics of the associated error

The error in the coupling due to the first-order reflection is defined, in decibels, as

$$dB_{error}=20\log_{10}\left(\left|1+\frac{V_1}{V_0}\right|\right)=20\log_{10}\left(\left|1+\Delta_1\right|\right)=10\log_{10}\left(1+2\left|\Delta_1\right|\cos\phi_1+\left|\Delta_1\right|^2\right), \tag{33}$$

where ϕ_1 is the phase of Δ_1. As shown above, the phase of Δ_1 is essentially the phase of the product of the two reflection coefficients. In a specific instance, the phase of the reflection coefficients might be estimated with some certainty, but without additional information, it is reasonable to assume these phases are uniformly distributed within the ensemble of all possible situations.

Taking the phase of Δ_1 to be a uniform random variable such that $-\pi \le \phi_1 < \pi$, the error in decibels will be in the range

$$20\log_{10}\left(1-\left|\Delta_1\right|\right) \le dB_{error} \le 20\log_{10}\left(1+\left|\Delta_1\right|\right), \tag{34}$$

which is plotted in Figure 9. Values outside this range will not occur.

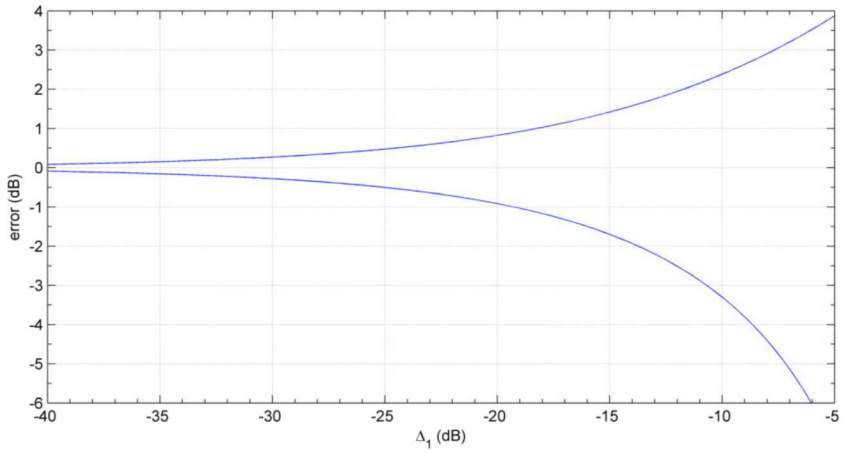

Figure 9 *Range of the error in coupling due to first-order reflection, in decibels, as a function of reflection amplitude.*

With the range of ϕ_1 as stated, and using the principal value of the inverse cosine, the dB_{error} function in (33) can be inverted to give

$$\phi_1\left(dB_{error},\Delta_1\right) = \pm\arccos\left(\frac{10^{dB_{error}/10}-1-\left|\Delta_1\right|^2}{2\left|\Delta_1\right|}\right). \tag{35}$$

The probability that the error is below a specified value, dB_{error} is the probability that ϕ_1 is less than $-\left|\phi_1\left(dB_{error},\Delta_1\right)\right|$ plus the probability that it is greater than $\left|\phi_1\left(dB_{error},\Delta_1\right)\right|$. Since ϕ_1 is uniformly distributed, the cumulative probability distribution for dB_{err} is

$$P\left(dB_{error}\right) = \begin{cases} 0, & dB_{error} \le 20\log_{10}\left(1-\left|\Delta_1\right|\right) \\ \dfrac{1}{\pi}\arccos\left(\dfrac{1+\left|\Delta_1\right|^2-10^{dB_{error}/10}}{2\left|\Delta_1\right|}\right), & 20\log_{10}\left(1-\left|\Delta_1\right|\right) < dB_{error} < 20\log_{10}\left(1+\left|\Delta_1\right|\right) \\ 1 & dB_{error} \ge 20\log_{10}\left(1+\left|\Delta_1\right|\right) \end{cases} \tag{36}$$

The probability density function for the error is discontinuous, bimodal, and strongly peaked near the extremes of (33), and is given by

$$p(dB_{error}) = \frac{\partial}{\partial dB_{err}} P(dB_{error})$$

$$= \begin{cases} \dfrac{\ln(10)}{20\pi} \dfrac{10^{dB_{err}/10}}{\sqrt{|\Delta_1|^2 - \frac{1}{4}\left(1 + |\Delta_1|^2 - 10^{dB_{err}/10}\right)^2}} & \text{for } 20\log_{10}\left(1 - |\Delta_1|\right) < dB_{error} < 20\log_{10}\left(1 + |\Delta_1|\right) \\ 0 \text{ otherwise} \end{cases} . \quad (37)$$

The cumulative probability distribution and probability density are plotted in Figure 10 for the case when $|\Delta_1| = -25$ dB. As already noted, the probability density is highest at the extremes of the distribution. In addition, as the error term becomes larger, the probability functions become more skewed away from zero error, and their shapes are less symmetrical. For example, compare the case of $|\Delta_1| = -25$ dB in Figure 10 with the case of $|\Delta_1| = -10$ dB in Figure 11.

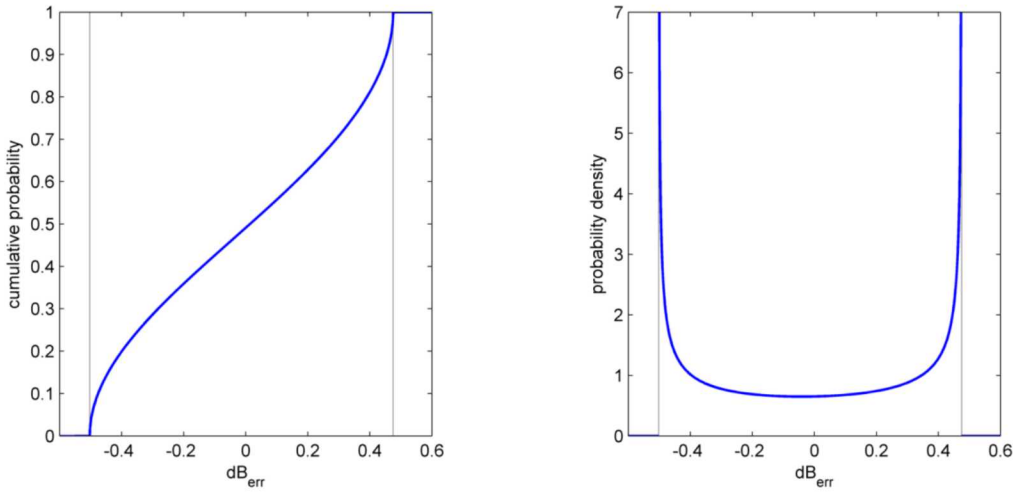

Figure 10 Cumulative probability distribution (left) and probability density (right) for the error caused by the first reflection when $|\Delta_1| = -25$ dB.

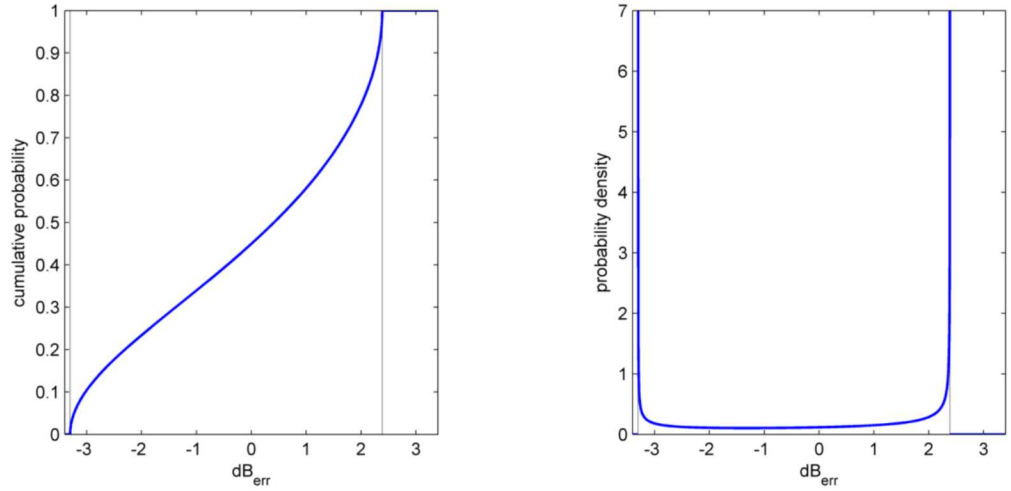

Figure 11 Cumulative probability distribution (left) and probability density (right) for the error caused by the first reflection when $|\Delta_1| = -10$ dB.

An example

Using the analytic model derived above for radiation from a point current source, the spatial-frequency response along the z axis can be computed. For the purpose of illustration, the following parameters are applied to the model:

$\Gamma_{aut} = -0.70$ $\quad z_{min} = 30$ inches $\quad f_{min} = 2$ GHz

$\Gamma_{probe} = -0.70$ $\quad z_{max} = 60$ inches $\quad f_{max} = 4$ GHz

The amplitudes of the real and imaginary parts of the normalized field are displayed in Figure 12 as a function of temporal frequency (vertical axis) and position along the z axis (horizontal axis).

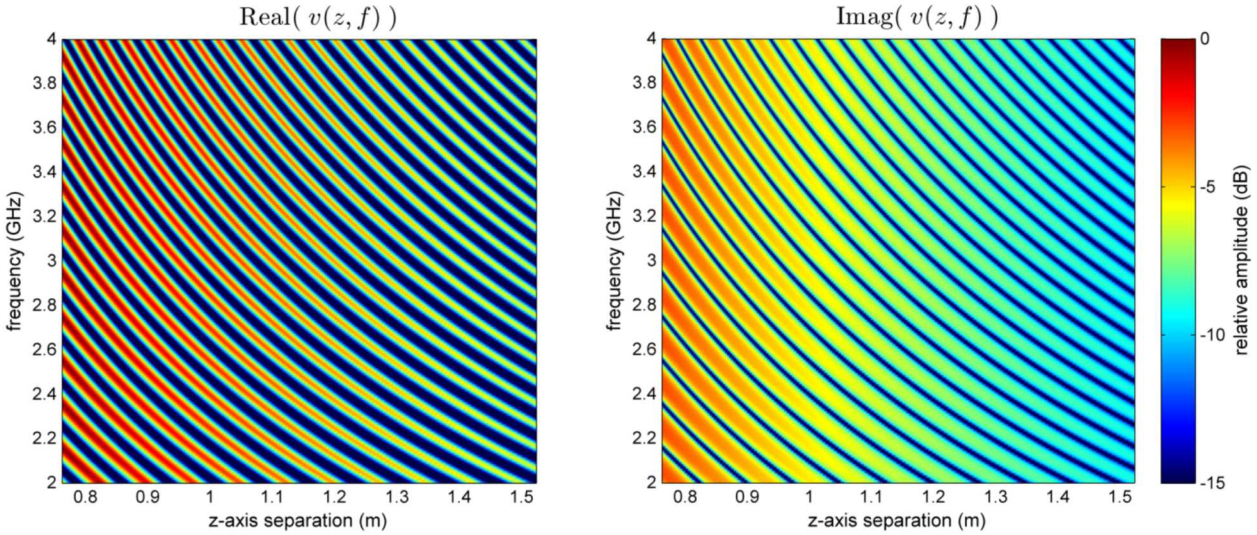

Figure 12 Real (left) and imaginary (right) response along the z axis for the example.

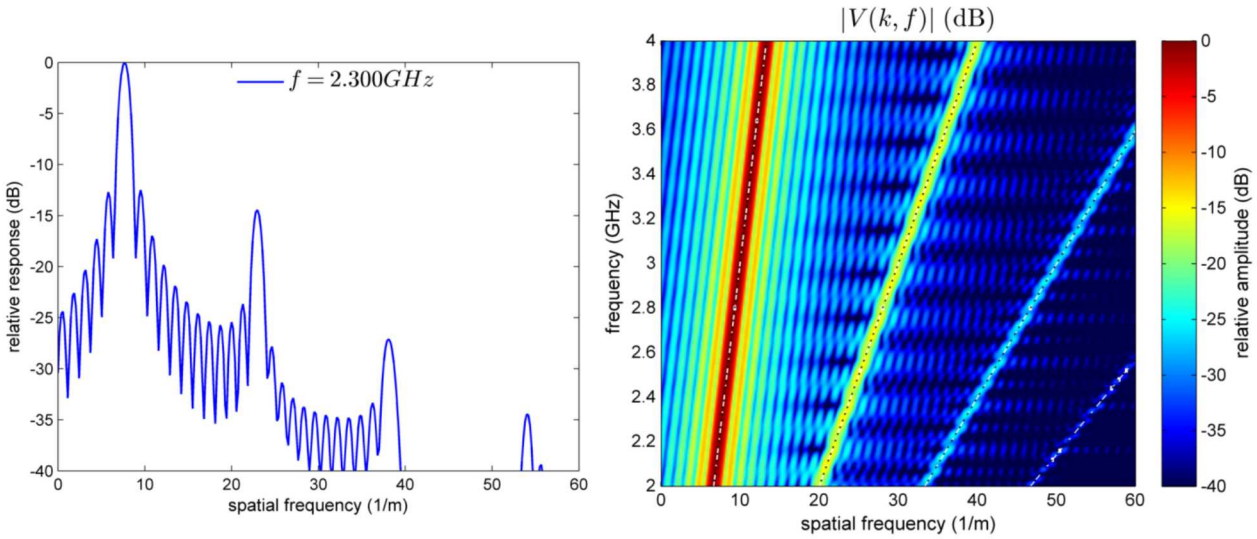

Figure 13 Normalized spatial-frequency response along the z axis for the example, for single frequency, at $f = 2.3$ GHz, at left, and over the entire bandwidth, $2 \le f \le 4$ GHz, at right.

The spatial-frequency response for the single frequency $f = 2.3$ GHz is plotted on the left in Figure 13. The plot on the right of Figure 13 shows the response for all temporal frequencies in the range

$2\ \text{GHz} \le f \le 4\ \text{GHz}$, with the broken lines indicating where the expected peak responses of the direct coupling and successive reflections occur. The left-most peak represents the direct coupling, while the peaks progressively to the right represent the 1st, 2nd, and 3rd reflections. In this example, choosing the reflection coefficients to be fairly large for both the probe and antenna under test allows these higher-order reflections to be seen clearly. No processing weight has been applied to reduce spatial-frequency side lobes caused by the truncation of the Fourier transform at finite limits. The sidelobes are easily identified with the direct coupling or various order reflections according to their slopes with respect to temporal frequency (see the plot on the left of Figure 13). Interference among the several terms is apparent at higher spatial frequencies as the reduced intensity of the response competes with side lobes from the direct-coupling response.

This example, based on the analytic model, demonstrates that the relative response of the significant reflections between the antenna under test and the probe can be isolated and measured by processing the measured amplitude and phase response obtained while moving the probe, or the antenna, along the z axis. With measured data, a numerical fast-Fourier-transform (FFT) algorithm would be applied, and the sampling interval along the z axis must be chosen to avoid aliasing of the highest-order reflection anticipated to be present. As has been shown in Figure 13, the process can be applied equally well to a narrow-bandwidth measurement (single frequency), or to a wide-bandwidth measurement with many frequencies. The width of the response lobe (resolution) is determined by the distance, measured in wavelengths, along the z axis for which data is obtained. Sidelobes can be reduced by applying an appropriate weighting function to the data before performing the numerical Fourier transform. The spatial-frequency resolution is reduced as the sidelobes are reduced, but increasing the length along the z axis for which the data is collected can mitigate this loss of resolution.

Extending the model to include other reflections

The behavior of reflections between the antenna and probe has been examined, and it has been demonstrated that these reflections can be detected and evaluated with the z-axis spatial-frequency analysis. However, additional reflections can occur from objects or structures located to the side of either the antenna or probe, but which move with the antenna or probe. Other reflections from stationary surfaces will also occur. These reflections will behave somewhat differently than the reflections that occur directly between the probe and antenna, as a consequence of their different propagation paths, and this behavior needs to be examined.

Reflections from structures extending to the sides of the probe or antenna

Suppose the antenna and/or probe has structural parts that extend to the sides, in a direction transverse to the z axis. For example, consider the structure attached to the antenna in Figure 14. For the path indicated in the illustration, the length traversed by the n^{th} reflection between this structure and the probe and back to the antenna is

$$L_n = z + 2n\sqrt{z^2 + d^2}\ , \tag{38}$$

where d is the distance in the x-y plane to the point of reflection.

The rate of change of this path as the distance between the probe and antenna changes is

$$\frac{d}{dz} L_n = 1 + 2n \frac{z}{\sqrt{z^2 + d^2}}\ . \tag{39}$$

Since the path length for the n^{th} reflection occurring directly between the antenna and probe is $(2n+1)z$, its rate of change is simply $2n+1$. It is this rate of change of the path length that determines the spatial frequencies present in the response component due to the reflection. Since

$$\frac{d}{dz}L_n < 2n+1\,, \tag{40}$$

the spatial frequencies associated with reflections from objects offset to the side, but which move with the antenna or probe, will always be *less* than the spatial frequencies associated with the same order reflection occurring directly between the antenna and probe. Additional reflection paths, other than the one shown in Figure 14, are possible. A little thought will show that the above statement is also true for spatial frequencies associated with those paths. The analysis is similar to what has already been presented, and will not be detailed here.

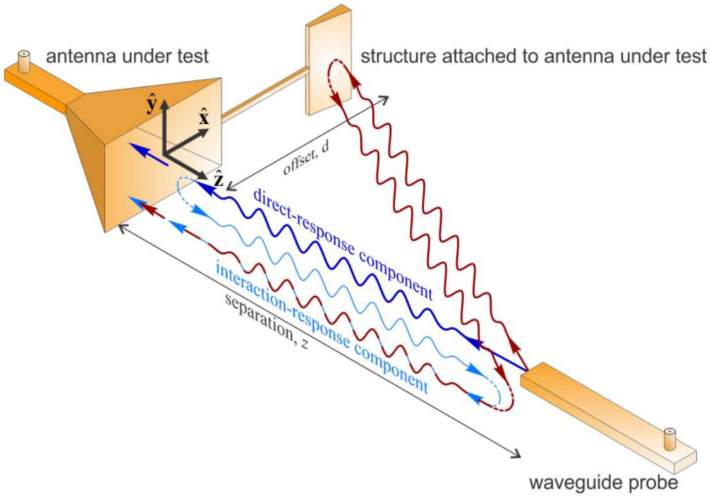

Figure 14 Illustration of the reflection path from the probe to a structure attached to the antenna under test.

Reflections from stationary side walls of the measurement room

Many possibilities exist for interactions between stationary objects, the probe, and the antenna under test, so for simplicity, a somewhat idealized situation will be analyzed. Figure 15 shows the geometry associated with a direct reflection from a single side wall[4]. The analysis applies equally for similar reflections from other surfaces, including the floor, ceiling, positioner table or slide, etc.

To simplify the analysis, the reflection from the side wall will be assumed to behave essentially as a specular reflection, so the point of reflection can be taken to be on the wall halfway between the antenna and probe. Additionally, multiple reflections can occur, complicating the situation considerably, as many paths are possible for the subsequent reflections. To minimize complexity, while still providing insight into the behavior of multiple reflections, only multiple reflections following the same path as the first reflection will be considered in the analytic model below. For interactions with the wall along the path depicted in red in Figure 15, the additional contribution to the received voltage will be modeled as

$$v_{wall}(z) = \sum_{n=1}^{\infty} v_n(z) = C'' \sum_{n=1}^{\infty} \Gamma_{wall}^{(2n-1)} \Gamma_{aut}^{n-1} \Gamma_{probe}^{n-1} \frac{e^{-jk_0(2n-1)L}}{4\pi(2n-1)L}\,, \tag{41}$$

where L is the total length of the one-way propagation path, via the wall, between the probe and antenna,

$$L = 2\sqrt{d^2 + \frac{1}{4}(z - z_0)^2}\,, \tag{42}$$

n indicates the number of times the signal reflects along the path, C'' accounts for the antenna and probe gains, Γ_{wall} is the reflection coefficient associated with the wall, and z_0 locates the aperture of the antenna.

[4] The various on-axis reflections from the end walls will behave similarly to the direct coupling or the direct reflections between the probe and antenna. This is a consequence of their total path length changing at the same rate as the path between the probe and antenna as the separation distance is varied.

This path is assumed long enough to justify including only the field terms that are inversely proportional to the path length in the analysis. The higher-order reflections $(n>1)$ include reflections from the antenna and probe. The reflection coefficients associated with the antenna and probe, Γ_{aut} and Γ_{probe} are functions of angle, and therefore may have different values than for the direct reflections between the antenna and probe, but that angular dependence is not explicitly shown in the equations describing the model. While the summation is written as an infinite sum, the product of reflection coefficients can rapidly become so small as to be negligible in a well-designed anechoic chamber, allowing the summation to be truncated to a few or even a single term.

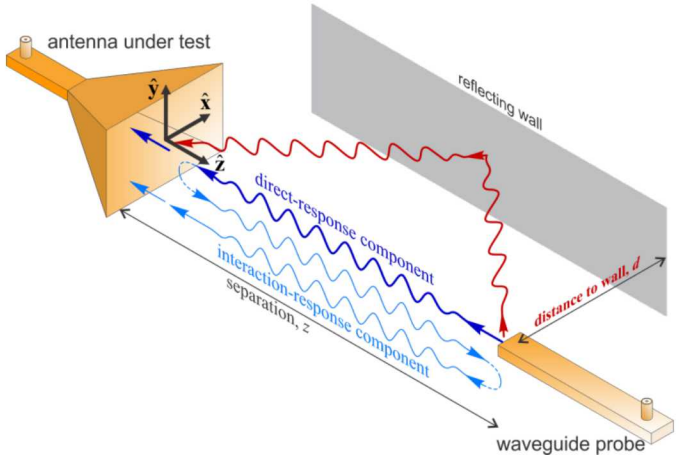

Figure 15 Illustration of a reflection from a side wall from the probe to the antenna, in addition to the direct-response component and the interaction-response that has previously been examined.

In an effort to anticipate the behavior of the side-wall reflection, consider the rate of change of L with respect to z,

$$\frac{dL}{dz}=\frac{\left(z-z_0\right)}{\sqrt{\left(z-z_0\right)^2+4d^2}}\ . \tag{43}$$

For any values of z, z_0, and $d>0$, it will always be the case that $\left|dL/dz\right|<1$, so L changes at a lower rate than the separation between the antenna and probe, and thus the first ($n=1$) reflection will produce a response at a *lower* spatial frequency than the direct coupling between the probe and antenna. As the distance to the wall increases, the associated spatial frequency for the first side-wall reflection becomes even lower. This is a crucial difference between the behavior of interactions with the wall and the behavior of the antenna-to-probe interactions. For example, when $z-z_0=60$ inches and $d=120$ inches, $dL/dz\simeq 0.24$, the response from the first side-wall reflection will occur at roughly a fourth of the spatial frequency associated with the direct response. For a longer wall distance, $d=240$ inches, the rate of change is $dL/dz\simeq 0.126$. It will be shown below that, as with multiple reflections between the probe and antenna, multiple reflections from the wall will produce higher spatial frequencies than the single reflection. Nevertheless, in a well-designed near-field range, the second and subsequent reflections should be negligible in comparison to the first.

Continuing with the simplified analysis, the spatial-frequency response associated with the n^{th} wall reflection is obtained from the Fourier integral

$$V_{wall,n}(k)=\int_{z_{min}}^{z_{max}} v_n(x)e^{jkz}dz = C''\Gamma_{wall}^{(2n-1)}\Gamma_{aut}^{n-1}\Gamma_{probe}^{n-1}\int_{z_{min}}^{z_{max}} \frac{e^{-j\left(k_0 2(2n-1)\sqrt{d^2+\frac{1}{4}(z-z_0)^2}-kz\right)}}{8\pi(2n-1)\sqrt{d^2+\frac{1}{4}(z-z_0)^2}}dz\ , \tag{44}$$

for which an exact closed-form expression is not readily available. An approximate form can be obtained by expanding the square root in (44) in a series[5],

$$\begin{aligned}\sqrt{d^2+\frac{1}{4}(z-z_0)^2} &= d\left(1+\frac{1}{2}\left(\frac{z-z_0}{2d}\right)^2-\frac{1}{8}\left(\frac{z-z_0}{2d}\right)^4+\frac{1}{16}\left(\frac{z-z_0}{2d}\right)^6+\cdots\right)\\ &= d\sum_{n=0}^{\infty}(-1)^{n-1}\frac{(2n-3)!!}{(2n)!!}\left(\frac{z-z_0}{2d}\right)^{2n}.\end{aligned} \tag{45}$$

The series in (45) only converges for $d>|z_0-z|/2$. When the distance to the wall is large with respect to the maximum excursion of z from z_0, keeping only the first term of (45) in the denominator of the integrand and the first two terms in the exponential gives the following approximation to the received voltage due to the n^{th} wall reflection,

$$V_{wall,n}(k)=C''\frac{\Gamma_{wall}^{(2n-1)}\Gamma_{aut}^{n-1}\Gamma_{probe}^{n-1}}{8\pi(2n-1)d}\int_{z_{min}}^{z_{max}} e^{-j\left(2k_0 d(2n-1)\left(1+\frac{1}{2}\left(\frac{z-z_0}{2d}\right)^2\right)-kz\right)}dz\ . \tag{46}$$

The integral can be evaluated in terms of the Fresnel integrals, plotted in Figure 16, and which are defined as [7]

$$C(x)=\int_0^x \cos\left(\frac{\pi}{2}t^2\right)dt \quad \text{and} \quad S(x)=\int_0^x \sin\left(\frac{\pi}{2}t^2\right)dt\ . \tag{47}$$

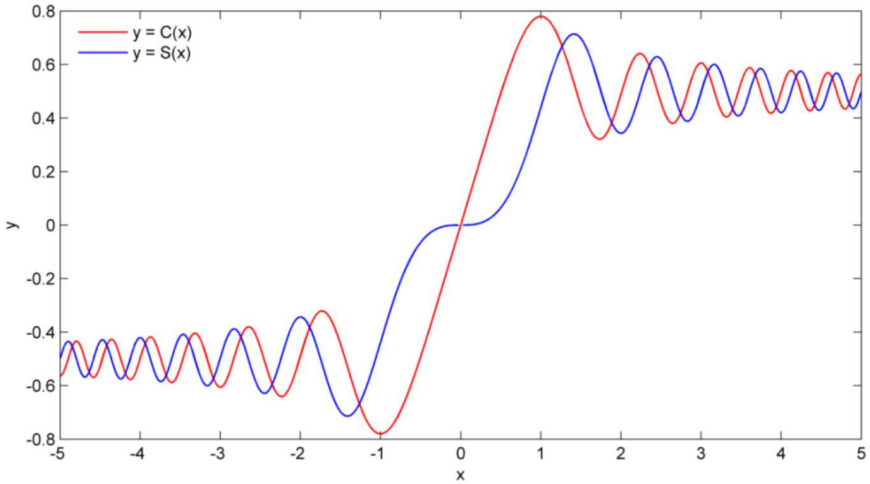

Figure 16 Fresnel integrals that describe the response from the wall.

The result of integrating (46) is the spatial-frequency-domain contribution from the n^{th} wall reflection, and is

[5] The double factorial notation means $2n!!=2\cdot4\cdot6\cdots(2n)=2^n n!$ and $(2n-1)!!=1\cdot3\cdot5\cdots(2n-1)=2^n\Gamma\left(n+\frac{1}{2}\right)/\sqrt{\pi}$, (see 6.1.49 in [7]).

$$V_{wall,n}(k) \simeq -C'' \Gamma_{wall}^{(2n-1)} \Gamma_{aut}^{n-1} \Gamma_{probe}^{n-1} \frac{e^{-j\left(2k_0 d(2n-1) - \frac{k^2}{k_0(2n-1)} d - kz_0\right)}}{4\sqrt{2\pi k_0 d(2n-1)^3}} \begin{Bmatrix} C(\kappa(k, z_0 - z_{max})) - jS(\kappa(k, z_0 - z_{max})) \\ -C(\kappa(k, z_0 - z_{min})) + jS(\kappa(k, z_0 - z_{min})) \end{Bmatrix}, \quad (48)$$

where

$$\kappa(k,z) = \sqrt{\frac{2k_0 d}{\pi(2n-1)}} \left(\frac{k}{k_0} - (2n-1)\frac{z - z_0}{2d} \right). \quad (49)$$

Since the Fresnel integrals are bounded, $-0.78 < C(x) < 0.78$ and $-0.72 < S(x) < 0.72$, the magnitude of the left-most factor in (48) never exceeds about 2.1. This means that the importance of the n^{th} reflection relative to the first reflection can be estimated by the proportionality

$$\frac{\left|V_{wall,n}(k)\right|_{\max}}{\left|V_{wall,1}(k)\right|_{\max}} \propto \frac{\Gamma_{wall}^{2(n-1)} \Gamma_{aut}^{n} \Gamma_{probe}^{n}}{\sqrt{(2n-1)^3}}. \quad (50)$$

Clearly, the $n = 1$ component will be dominant, particularly when the reflection coefficient of the wall is small, as it is in an anechoic chamber. It can be shown that $\left|V_{wall,n}(k)\right|$ has extrema at

$$k = (2n-1)k_0 \frac{(z_{max} + z_{min} - 2z_0)}{4d} + m\frac{2\pi}{z_{max} - z_{min}}, \; m \in Integers. \quad (51)$$

The maximum for the first reflection ($n = 1$) occurs when $m = 0$, so the spatial frequency of the first-reflection peak is

$$f_s = \frac{(z_{max} + z_{min} - 2z_0)}{4d} \frac{f_0}{c}, \quad (52)$$

which, for $d > (z_{max} + z_{min} - 2z_0)/4$, will always occur at a spatial frequency lower than the direct coupling.

An example of the wall response alone, comparing the first reflection to the sum of the first four reflections is plotted in Figure 17. For this example, $k_0 = 2\pi$, $d = 20$, $z_0 = 5$, $z_{min} = 8$, $z_{max} = 16$, and $\Gamma_{wall} = \Gamma_{aut} = \Gamma_{probe} = -1$. Since it is unlikely that the magnitude of the reflection coefficients will be unity, the higher-order reflections will be even less significant than indicated in the figure.

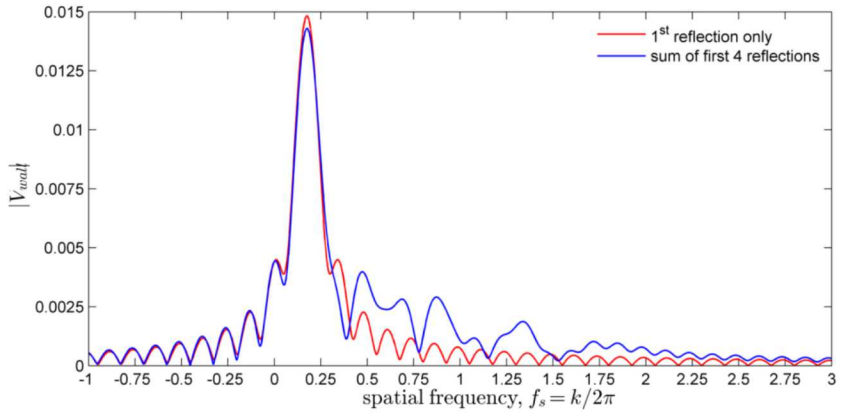

Figure 17 Comparison of response due to first wall reflection and sum of first four reflections, for parameters $k_0 = 2\pi$, $d = 20$, $z_0 = 5$, $z_{min} = 8$, $z_{max} = 16$, $\Gamma_{wall} = \Gamma_{aut} = \Gamma_{probe} = -1$.

An example with probe-to-antenna interaction and side-wall reflections

The model for the side-wall reflection is added to the antenna-to-probe interaction model previously described. The composite response is examined for the following set of parameters:

$$\Gamma_{aut} = -0.70 \qquad z_0 = 0 \text{ inches} \qquad d = 144 \text{ inches}$$
$$\Gamma_{probe} = -0.70 \qquad z_{min} = 30 \text{ inches} \qquad f_{min} = 2 \text{ GHz}$$
$$\Gamma_{wall} = -1.00 \qquad z_{max} = 60 \text{ inches} \qquad f_{max} = 4 \text{ GHz}$$

The amplitudes of the real and imaginary parts of the normalized total coupling between the probe and antenna are plotted as a function of z-axis position and temporal frequency in Figure 18, on the left and right, respectively. In this case, interference between the various terms is very evident in the form of ripples along the peak-response ridges.

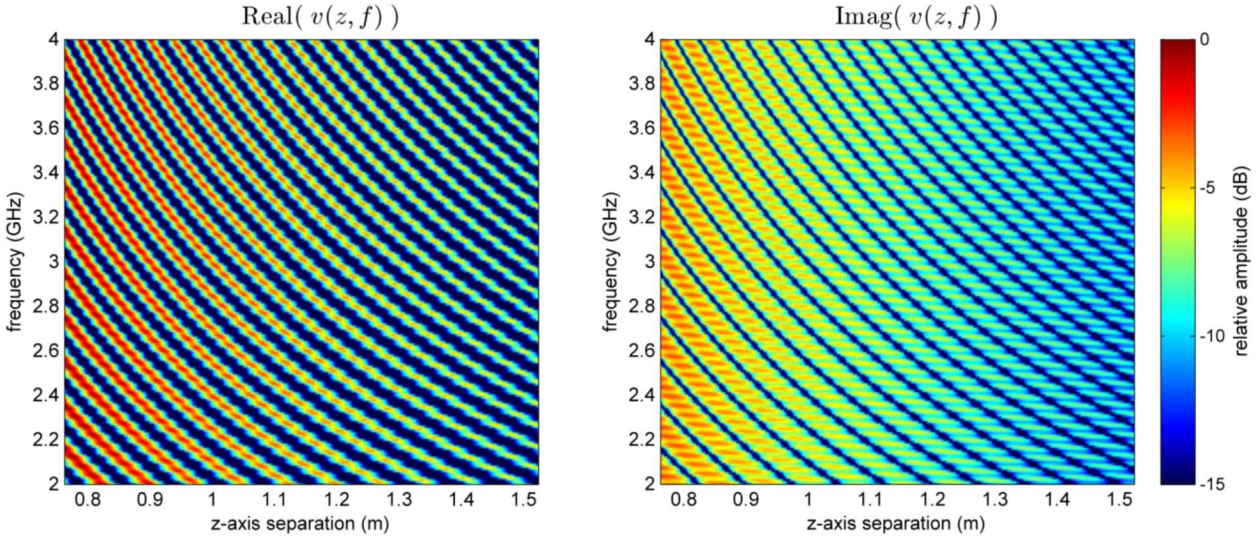

Figure 18 *Real and imaginary response along the z axis for the example with the addition of the wall response.*

The resulting normalized spatial-frequency response for $f = 2.3$ GHz is plotted on the left in Figure 19, while the spatial-frequency response for the complete range of temporal frequencies is plotted on the right. In all cases, the amplitudes are normalized to the direct coupling at each temporal frequency. The peak of the spatial frequency associated with the reflection from the wall should occur at about $f_s = 0.16\dfrac{k_0}{2\pi}$, well below that of the direct response, even though the propagation path is much larger. However, in Figure 19, the peak of the wall response for $f = 2.3$ GHz occurs at a slightly lower spatial frequency than predicted by (51). This is a result of the interaction of the side lobes of the direct response and the wall response. The full-band plot on the right of Figure 19 shows this effect, which is manifest in the ripple and variations seen along the peak-response ridge associated with the wall.

It is worth mentioning that if a time-domain analysis could be used, the response associated with the wall would appear to the right of the direct response instead of to its left because of the increased delay associated with the longer path length.

These examples are based on the simplified analytic models, which were derived above. As part of the simplification, no weighting was applied to the response function in order to suppress side lobes resulting from the Fourier transform integral over the finite range of z.

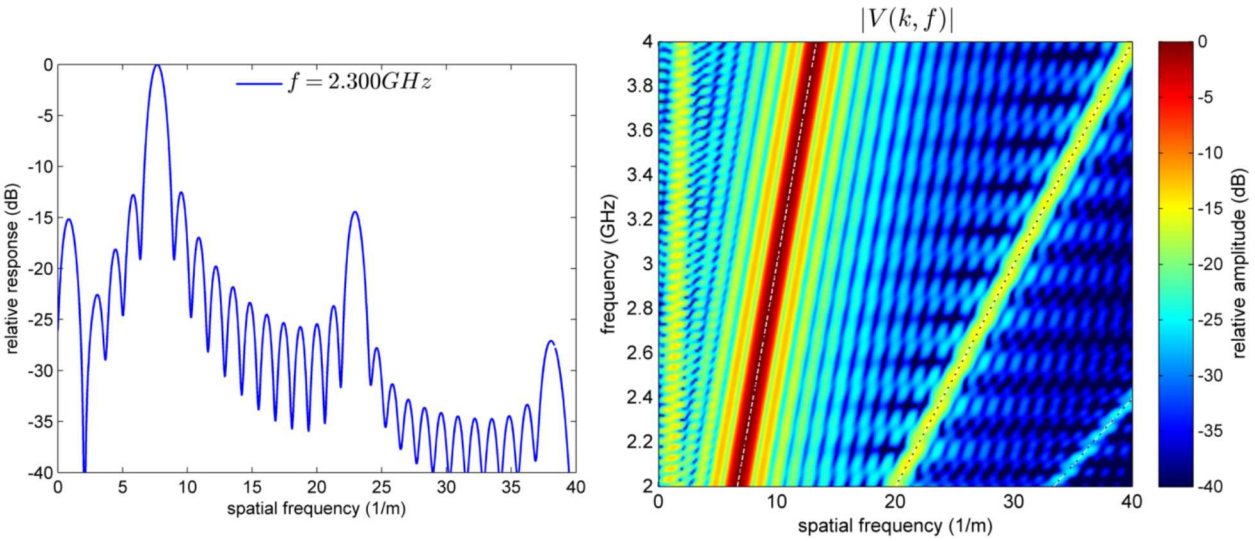

Figure 19 *Normalized z-axis spatial-frequency response for the same example as in Figure 12 and Figure 13, but with the addition of the wall response. The single-frequency response at* $f = 2.3$ GHz *is on the left, and the response over the frequency range* $2 \le f \le 4$ GHz *is on the right. The peak nearest the left is the response from the wall, while the largest response just to the right is the direct response. The two additional peaks to the right are the* 1^{st} *and* 2^{nd} *reflections, respectively.*

Summary of the spatial-frequency analysis

The spatial-frequency analysis will produce a peak response from the n^{th} reflection between the probe and the antenna under test at the approximate spatial frequency given by

$$f_s \approx (2n+1)\frac{f}{c}. \tag{53}$$

The location of the peak is approximate because the assumption has been made in the analysis that the reflection occurs at a point along the z axis, in particular from the center of the aperture. In reality, significant reflections could occur from structures located slightly offset from the z axis and at distances other than the location of the aperture, but still attached to the probe or antenna. It has been shown that reflections from such structures will produce lower spatial frequencies than given by (53).

The analysis of the side-wall reflection showed that the first reflection from a stationary wall can produce spatial frequencies somewhat lower than $1/\lambda$, simply because the rate of change of the phase along the reflection path is smaller than that of the direct coupling. The peak of the first reflection from a wall that is located a distance d from the z axis is expected to be near

$$f_s = \frac{(z_{max} + z_{min} - 2z_0)}{4d}\frac{f}{c}, \quad d > \frac{1}{4}(z_{max} + z_{min} - 2z_0). \tag{54}$$

Reflections from multiple surfaces in the measurement room can occur, but all dominant reflections from stationary side walls will occur in the region of spatial frequencies $f_s < f/c$, and multiple points of interaction can also cause the measured peak to be broadened or even broken into multiple peaks.

The spatial-frequency analysis for the probe-to-antenna interaction and the side-wall reflections can be applied with equal ease and accuracy to both narrow-bandwidth and wide-bandwidth antennas, unlike time-domain analysis, which requires very wide bandwidths to detect and isolate the various interactions. This makes spatial-frequency analysis a very powerful tool for detecting these interactions and assessing their impact on the uncertainty associated with the measurement.

Estimating the uncertainty using the spatial-frequency response

The models presented above are idealized. Even so, there is evidence of interference between side lobes associated with the direct response and the response associated with the reflections. This leads to variations in the amplitude of the reflection peaks as the temporal frequency is varied. In measured data, it is anticipated that there will be multiple points of reflection and additional sources of interference, which could cause significant variations. The result is that the peak response associated with each reflection component may not lie on a straight line relating spatial frequency to temporal frequency, as given by estimates for each reflection based on the analysis. In order to provide a good estimate of the amplitude of each reflection, it is necessary to search for the peak response in a region surrounding the expected location of the peak. The expected spatial frequencies of the probe-antenna interactions are based on the order of the reflection between the probe aperture and the antenna under test, while reflections from the stationary side-walls will occur at lower spatial frequencies than the direct response.

After the peaks of the reflections between the antenna and probe have been identified, the contribution to the gain uncertainty can be computed. For an uncertainty estimate, it is the relative amplitude of the various peaks with respect to the direct coupling that is relevant, not the absolute level. Thus, normalizing the response at each temporal frequency to the peak of the direct coupling is appropriate. In estimating this uncertainty over a band of temporal frequencies, it is desirable to smooth the data over the measured band, while providing a conservative estimate of the contribution to the uncertainty.

First, the mean, μ_f, and standard deviation, σ_f, of the peak-reflection responses can be computed over the set of temporal frequencies. Then, to obtain a smooth estimate of the total reflection component, the data is fit to the following polynomial function

$$s_{fit}(f) = \sum_{m=0}^{n} \alpha_m \left(\frac{f - \mu_f}{\sigma_f} \right)^m , \tag{55}$$

where the maximum degree, n, of the polynomial is a parameter that must be chosen with some judgment. Higher degree will allow the curve fit to follow the data better, but too large a degree can introduce wild fluctuations in the fit. By ensuring that the number of frequency points is significantly greater than the number of coefficients in the polynomial, the curve fit generally will be well constrained. It is recommended that the degree be chosen according to

$$n = \min\left(n_{max}, \lfloor n_f / n_s \rfloor\right), \tag{56}$$

where n_f is the number of temporal frequencies measured, n_s is a parameter specifying the number of frequency samples per degree, n_{max} is the upper limit on the degree to be allowed, and $\lfloor x \rfloor$ is the floor function, meaning the biggest integer less than or equal to *x*. For example, choosing $n_{max} = 15$ and $n_s = 10$ with $n_f = 91$ measured frequencies would suggest a degree of $n = 9$ for $s_{fit}(f)$.

The estimated uncertainty in the coupling, S_{21}, caused by reflections is

$$S_{21,meas} - \left(s_{fit} + 2\sigma_f\right) \le S_{21} \le S_{21,meas} + \left(s_{fit} + 2\sigma_f\right). \tag{57}$$

It will be instructive to examine these estimates for examples of measured data.

Examples of measured data

Several sets of data were collected on the large near-field range at the Sandia Facility for Antenna and Radar-cross-section Measurements (FARM). These data sets demonstrate the viability of the z-axis spatial-frequency analysis method for identifying and quantifying interactions between the antenna under

test and the near-field probe, as well as identifying and quantifying reflections from nearby structures, such as the side walls, floor, and ceiling.

Measurement showing first reflection

A set of S-band data was collected on April 24, 2012, with the bore-sight directions of the probe and antenna aligned as illustrated in Figure 2. The data set consists of measured values of S_{21} as the separation distance between the probe and antenna is varied. The probe is an MI-Tech WR-430 open-ended waveguide probe, and the antenna is an ARA S-band horn antenna (s/n 16581). The data spans a frequency range of 1.7 GHz to 2.6 GHz in 10-MHz steps, and the separation varies from 30 inches (0.762 m) to 100 inches (2.54 m) in nominal steps of 0.05 inches (1.3mm). At the lowest frequency, the separation varies from 4.32 wavelengths to 14.40 wavelengths, a change of about 10 wavelengths, while the interval between data points is 0.007 wavelengths. At the highest frequency, the separation varies from 6.61 wavelengths to 22.03 wavelengths, and the interval between data points is 0.010 wavelengths.

The data are calibrated by normalizing to the complex value of S_{21} obtained when the coaxial cables feeding the probe and antenna are connected together. This calibration process compensates for the variations in the frequency response of the instrumentation. Since this data was collected by the Orbit/FR software, the Agilent PNA was operating in an uncalibrated mode, meaning that internal coupling and leakage were not compensated. The magnitude of the coupling, in decibels, is plotted in Figure 20 as a function of frequency and lower-slide position[6]. The coupling exhibits a rapid decrease as the frequency moves to the lower end of the measured frequency band. The decrease in coupling as the separation is increased is also readily apparent.[7]

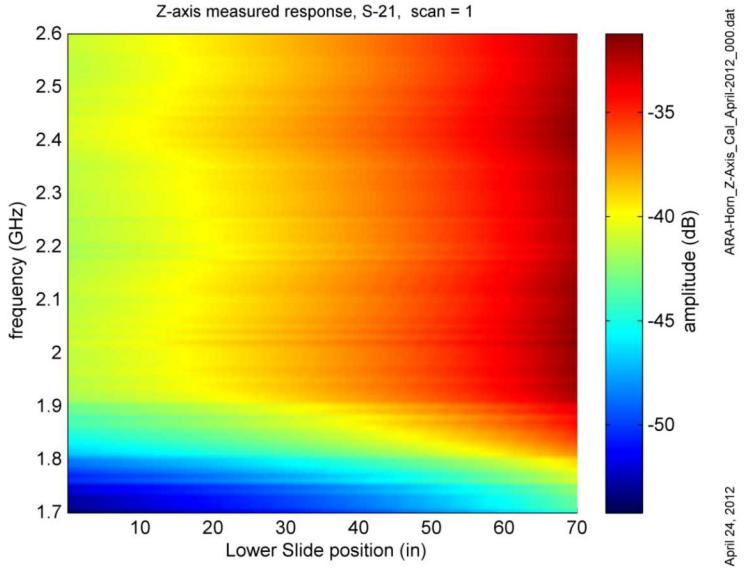

Figure 20 Magnitude of the measured coupling between the MI-Tech WR-430 open-ended waveguide probe and the ARA S-band horn antenna, in decibels.

[6] For this data set, and those that follow, the z-axis position is labeled "Lower Slide position" on the relevant plots. This is a value obtained from sensors on the slide, and which was recorded by the data-acquisition software. However, a possible sign change might need to be applied to the reported data, and an offset must be added to obtain the true distance between the aperture of the antenna and the aperture of the probe. This poses no problem or limitation for the analysis.

[7] For this measurement, the distance between the probe and the antenna's coordinate-system origin is obtained by subtracting the lower-slide position from 100 inches, so larger values of the lower-slide position correspond to shorter distances between the antenna and probe.

The real and imaginary parts of S_{21}, plotted in Figure 21, show clear and unambiguous phase variation as the separation is varied, which indicates a well-defined spatial frequency (cycles per meter) at each temporal frequency.

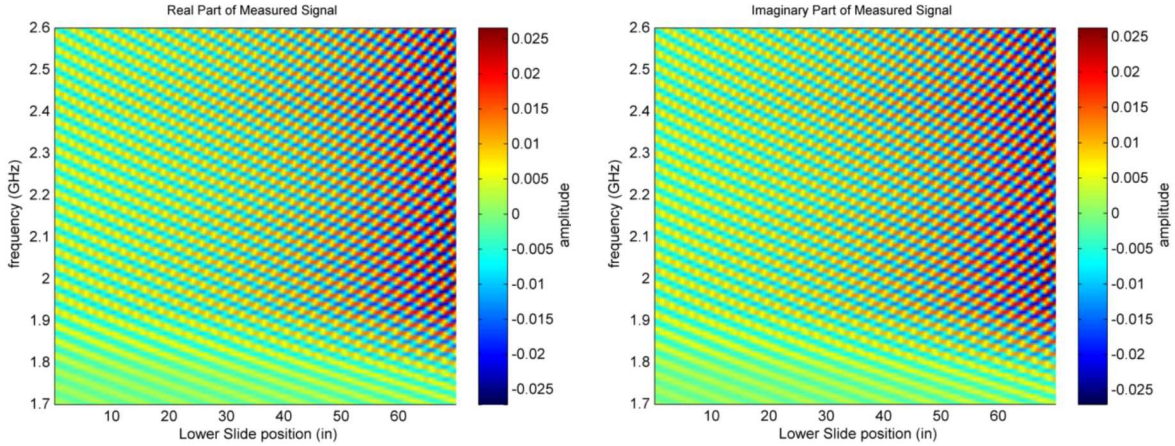

Figure 21 *Real (left) and imaginary (right) parts of the measured coupling between the probe and antenna. The vertical axis is frequency, and the horizontal axis is separation.*

The spatial frequency of the direct coupling is expected to be $1/\lambda$, where λ is the wavelength, but the first reflection between the horn and probe should have a spatial frequency of about $3/\lambda$, because its propagation path is three times as far. Similarly, the second reflection should have a spatial frequency of about $5/\lambda$. These estimates of the locations of the responses are somewhat inexact, since the reflections can come from various parts of the structures that are not directly on the z axis. Applying a Fourier transform in *z* will show the spatial frequencies present in the measured data, at each temporal frequency, independently of the expected positions. However, the expected positions provide a basis for where to look for the peak responses.

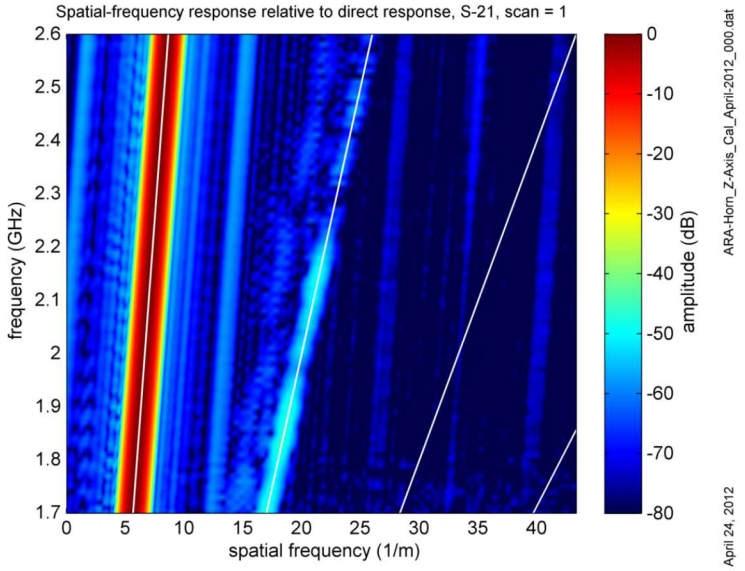

Figure 22 *Normalized spatial-frequency response associated with the reflection between MI-Tech WR-430 open-ended waveguide probe and the ARA S-band horn antenna. The white lines indicate the expected spatial frequencies for the direct coupling and first through third reflections, based on the analytic model.*

Figure 22 shows the spatial-frequency response as a function of temporal frequency that results from transforming the data displayed in Figure 20 and Figure 21 along the separation dimension, *z*. The response has been normalized to the direct response (red band) to obtain the relative response needed to compute the component of uncertainty. The expected positions of the various responses are shown as narrow white lines. The slope of the first reflection response is different from that of the direct coupling response, since it corresponds to triple the spatial frequency of the direct coupling. The direct coupling and first-reflection components are clearly visible in Figure 22, located at the expected positions, but there is no evidence of second or third reflections. At most frequencies, the peak of the first-reflection response does occur at the expected spatial frequency, although this reflection does not occur entirely between points on the z axis, as evidenced by smaller responses at lower spatial frequencies. Reflections occurring at points located away from the z axis are responsible for these. Sidelobes from the direct coupling are also apparent. The first reflection response is around 50 dB lower than that due to the direct coupling.

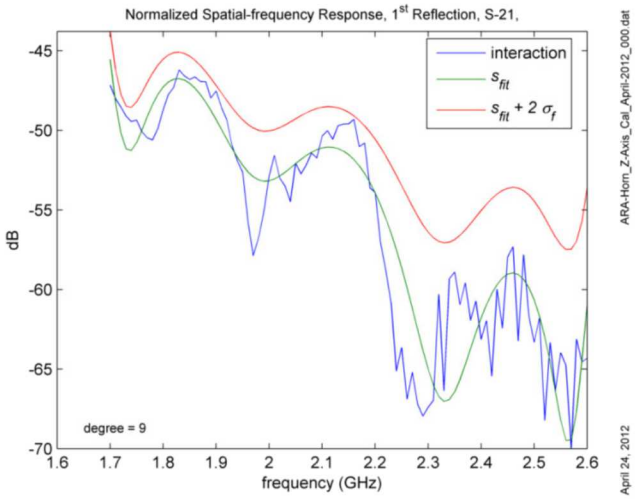

Figure 23 Normalized spatial-frequency response of the first reflection, with the 9th-order polynomial curve fit.

The peak of the first-reflection interaction response has been extracted and plotted in Figure 23 as a function of temporal frequency. The response is several tens of decibels below the direct coupling, and will contribute only a small amount to the uncertainty of the measured bore-sight gain. The slow variation with temporal frequency implies that there is more than a single interaction term, occurring at nearly the same spatial frequency, which produces the interference pattern seen in Figure 23. There is also a clear trend for the interaction response to decrease as frequency is increased.

The smooth fit, labeled s_{fit} in Figure 23, corresponds to an n^{th}-degree polynomial with $n = 9$. The polynomial is of the form (55), using (56) to choose the degree with $n_{max} = 15$ and $n_s = 10$ for $n_f = 91$ frequencies. A conservative estimate of the uncertainty of the direct coupling caused by reflections between the probe and the antenna is

$$S_{21,meas} - \left(s_{fit} + 2\sigma_f\right) \le S_{21} \le S_{21,meas} + \left(s_{fit} + 2\sigma_f\right). \tag{58}$$

The uncertainty bound for S_{21} due to the reflection between the probe and the antenna is plotted in Figure 24 for this example data set. In this case, the spatial-frequency analysis has shown that the interaction between the probe and antenna introduces only a small uncertainty in the bore-sight gain.

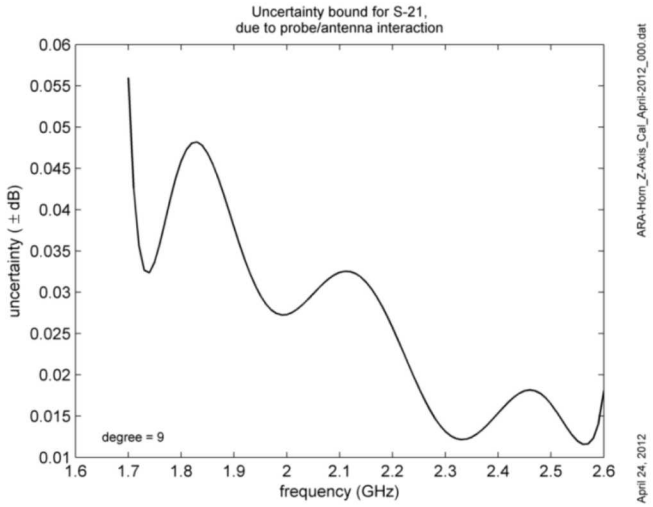

Figure 24 Boresight-gain uncertainty bound due to the presence of the first reflection.

The effect of varying the length of the z-axis excursion

The change in separation of the probe and antenna for this data set amounts to about 10 wavelengths at the lowest frequency. The effect of changing the range of separation between the probe and antenna can be seen in Figure 25, where the normalized spatial-frequency response is plotted for separation ranges of 10, 8, 5, and 2.5 wavelengths at the lowest frequency. The spatial-frequency resolution is reduced as the length of excursion is reduced, and the reduction of resolution becomes quite pronounced when the change in separation is reduced to only 2.5 wavelengths. The impact of the coarse resolution is the potential for confusing and smearing of various components of the response. In fact, for the small separation change of 2.5 wavelengths, detection of any response at spatial frequencies below those of the direct response is clearly impractical. This means that response due to side-wall reflections could not be adequately detected and quantified.

In Figure 25, the white lines indicate the expected location of the various contributions, based on the analytic model described above. The red lines indicate the bounds within which the search algorithm looks for the maximum value at each frequency, and the dashed lines indicate the location of the maximum values chosen for each temporal frequency. It is clear from examination of Figure 25 that the algorithm is much more adept at accurately selecting responses associated with the first reflection when the length of the excursion is larger. For example, for the smaller excursions, the algorithm confuses sidelobes or even the edges of the main lobe of the direct response with the response from the first reflection.

The contribution of the first reflection to the uncertainty is plotted in Figure 26 for the four different z-axis excursions. The 2.5-wavelength change severely over-estimates the uncertainty, compared to the longer z-axis excursions, and this is consistent with the circumstance that a large portion of the contributions chosen by the search algorithm were from the edge of the main lobe of the direct response. The agreement between the estimates with 5-, 8-, and 10-wavelength changes is more consistent. However, it is clear from Figure 25 that the 5- and 8-wavelengh z-axis excursions cause the search algorithm to confuse direct-response sidelobes with the first-reflection response. These data suggest that at least a 10-wavelength excursion should be used when practical.

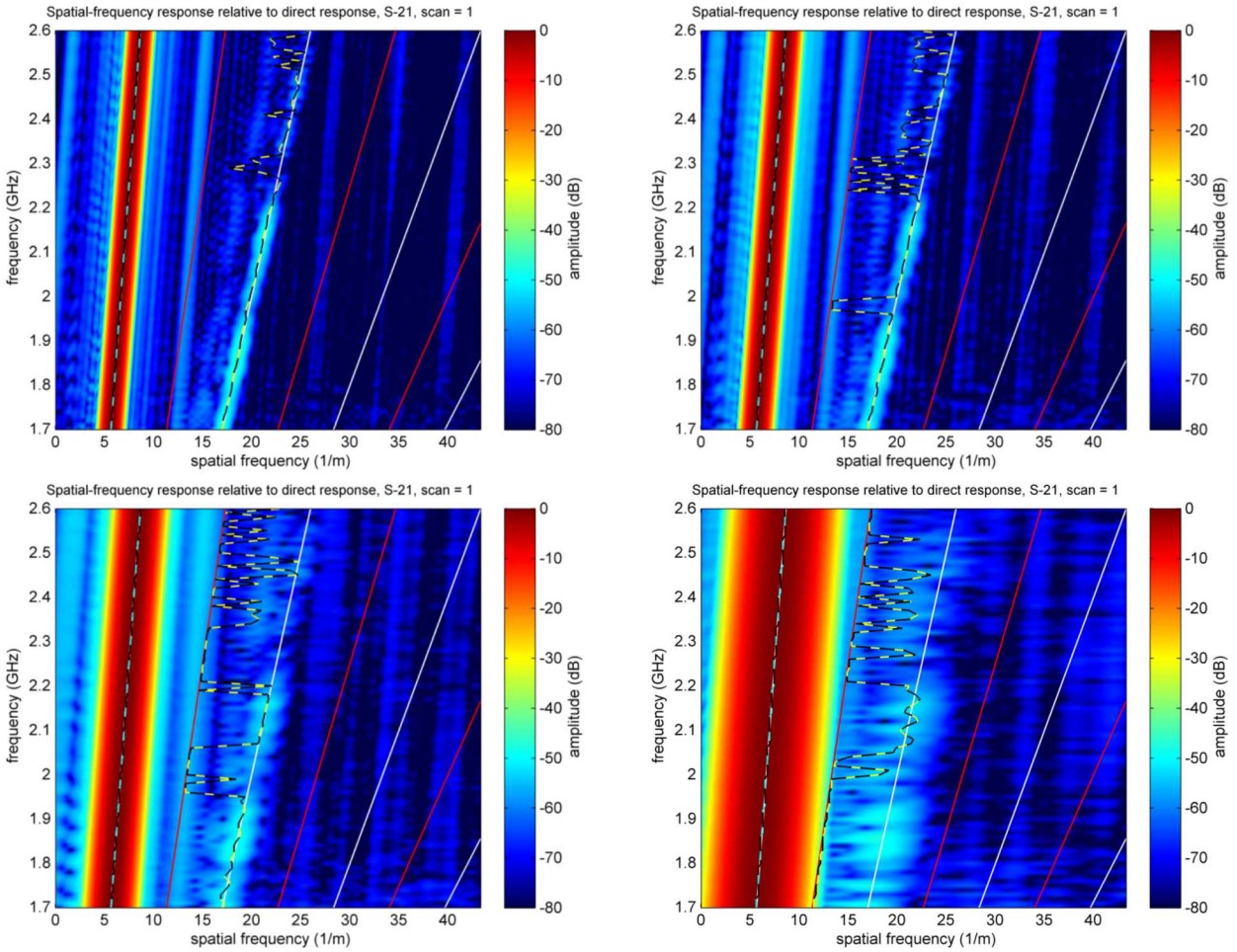

Figure 25 *Normalized spatial-frequency response when the separation between the probe and antenna is 10 wavelength (upper left), 8 wavelengths (upper right), 5 wavelengths (lower left), and 2.5 wavelengths (lower right). In all cases, the sample interval at the highest frequency is 0.01 wavelength.*

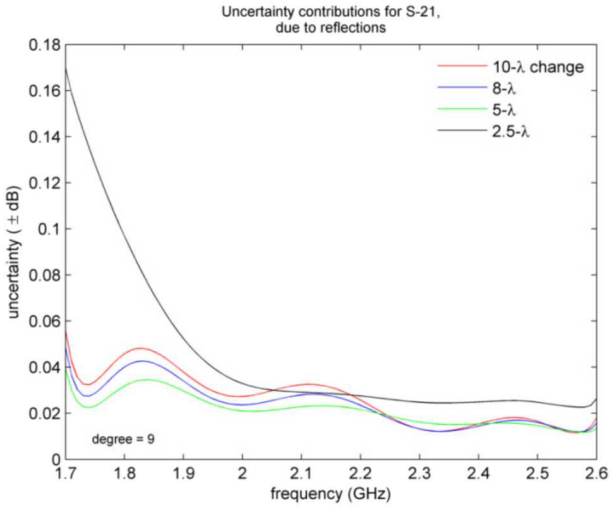

Figure 26 *Uncertainty estimates for z-axis separation changes of 10, 8, 5, and 2.5 wavelengths at the lowest frequency.*

Changing the bounds to narrow the region in which the algorithm searches for the peaks is certainly possible, and might make uncertainty estimates using shorter z-axis excursions more accurate by reducing the chance of mistakenly selecting sidelobe contributions. However, the reflections between off-axis portions of the probe and the antenna certainly can produce components at spatial frequencies below those expected from the analytical model (white lines), so narrowing the search region too much could cause some of these to go undetected. It might also be useful to change the weighting function to reduce the sidelobes[8], or it might even be possible to design a smarter search algorithm that can detect points associated with sidelobes. Nevertheless, making the z-axis excursion about 10 wavelengths at the lowest frequency provides good resolution and is a reasonable choice for many situations. Increasing the spatial-frequency resolution even more may be desirable when reflections from walls and other nearby stationary structures are significant. Since these will produce spatial frequencies below those associated with direct coupling, enhanced resolution may be necessary to adequately separate them.

The effect of varying the z-axis sample spacing

The effect of increasing the interval between spatial samples is examined next. Figure 27 shows the normalized spatial-frequency response with a sample spacing of 0.258 inches on the left and with a sample spacing of 0.698 inches on the right. As the temporal frequency varies from lowest to highest, this corresponds to 0.036 - 0.055 wavelengths and to 0.100 - 0.154 wavelengths for the two sample spacings. The z-axis excursion is 10 wavelengths at the lowest frequency. The effect of increasing the sample size along the z axis is simply to reduce the maximum spatial frequency that can be detected without aliasing. The image on the left of Figure 27, having more closely spaced samples along the z axis, has nearly three times the range of unaliased spatial frequencies compared to the image on the right.

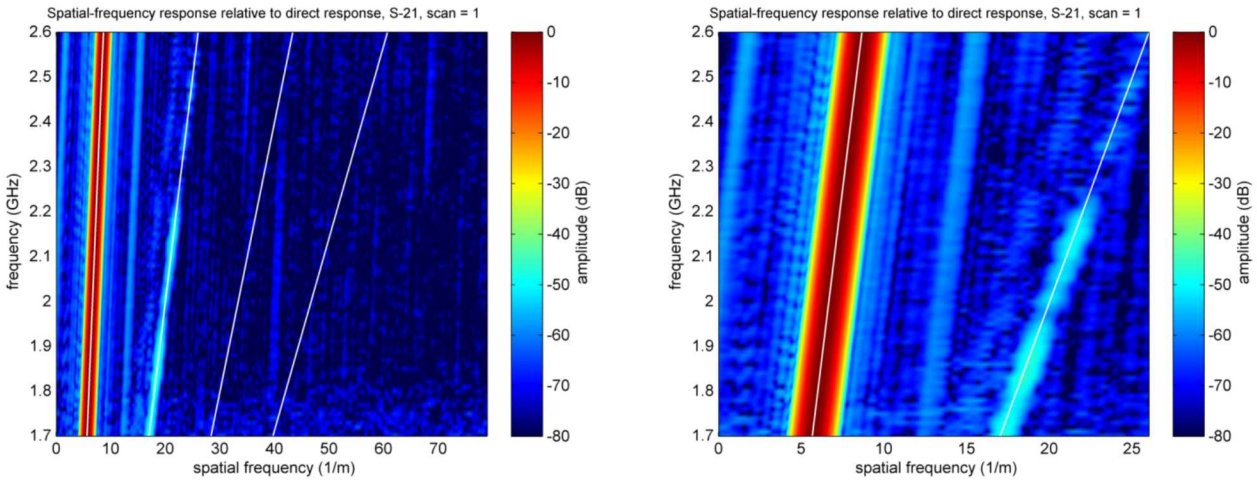

Figure 27 Normalized spatial-frequency response when the change in separation between the probe and antenna of 10 wavelengths, with the sample interval ranging from 0.036 to 0.055 wavelengths (left) and from 0.100 to 0.154 wavelengths (right) for the lowest and highest frequencies, respectively.

Since this analysis is based on the application of the discrete Fourier transform, the resolution in the spatial-frequency domain is determined by the total extent of the data in the spatial domain. Similarly the total extent of the transformed result in the spatial-frequency domain depends on the sample spacing (spatial-resolution) of the data in the spatial domain. These two principles are clearly demonstrated by the data displayed in Figure 25 and Figure 27.

[8] The weight function used in all of the processing reported here is a Taylor weighting with $\bar{n} = 21$ and $sll = -80$ dB.

Measurement showing second reflection

A second measurement was performed using the ARA horn and MI-Tech WR-430 open-ended waveguide probe, only this time absorber covering the probe's mounting structure was removed. Additionally, more frequencies, $n_f = 361$, were measured. This data spans a frequency range of 1.7 GHz to 2.6 GHz in 2.5-MHz steps. As with the first data set, the separation varies from 30 inches (0.762 m) at the 70-inch lower-slide position to 100 inches (2.54 m) at the 0 lower-slide position. The mean step size is 0.05 inches (1.3mm). At the lowest frequency, the separation varies from 4.32 wavelengths to 14.40 wavelengths, while the interval between data points is 0.0072 wavelengths. The magnitude of the measured response is plotted in Figure 28, where some ripple, consistent with the presence of interfering components, can be seen.

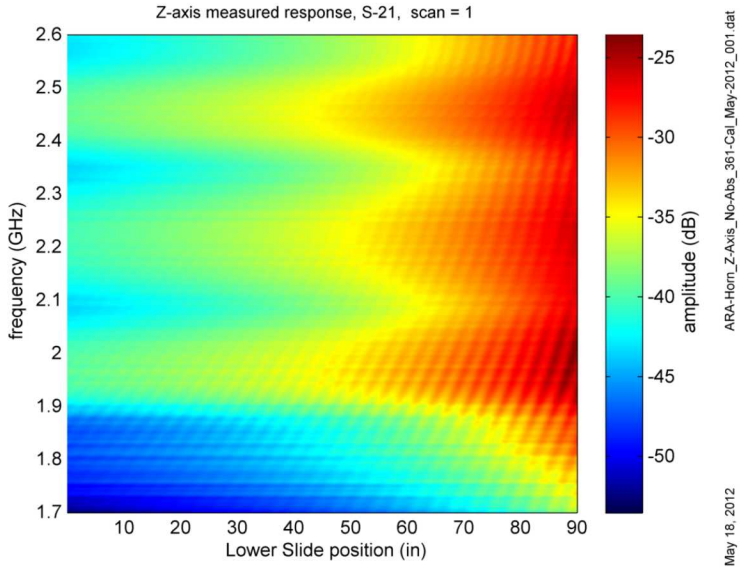

Figure 28 Magnitude of the measured coupling between the MI-Tech WR-430 open-ended waveguide probe and the ARA S-band horn antenna. The absorber has been removed from the probe mounting structure.

The spatial-frequency response is plotted in Figure 29, where the second-order reflection is clearly visible, being strongest in the temporal-frequency region around 1.9 GHz. The first-order reflection is also stronger than for the first set of data, Figure 22, and is very prominent around 1.9 GHz. Although the same probe and antenna were measured, the removal of absorber from the probe-support structure has made an obvious difference.

As observed from Figure 29, the peak of the first-reflection interaction response is considerably larger than the second-reflection response. The first- and second-reflection responses have been extracted with a peak-search algorithm and plotted in Figure 30 as a function of temporal frequency, along with a smooth polynomial fit to the response. In Figure 29, the dashed lines indicate the locations where the search algorithm picks the maxima of each of the direct, first-reflection, and second-reflection responses at each temporal frequency, while the white lines indicate the expected location, based on the analytic model. Notice that the algorithm bounces between the second-reflection response and a sidelobe of the direct response in regions were the response is very low. In order to not miss significant contributions, the search algorithm looks in a region centered along the expected position for each of the reflections, and when the contribution is low, it can pick values that are actually sidelobes from a another strong response. However, since these values are quite low, the contribution to the uncertainty is small, and the compromise is justified by the ability to not miss significant contributions that occur at spatial frequencies other than the nominal (expected) response.

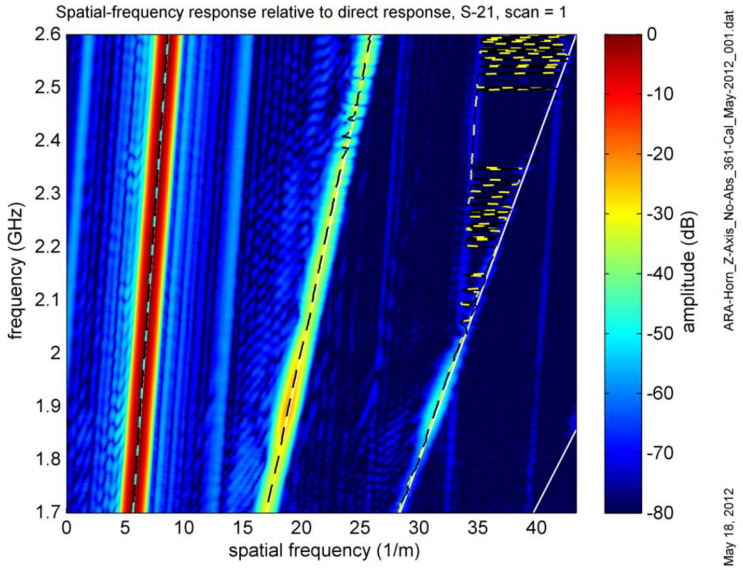

Figure 29 *Normalized spatial-frequency response obtained from the data plotted in Figure 28. The second-order reflection is clearly present, and most visible in the temporal-frequency region around 1.9 GHz.*

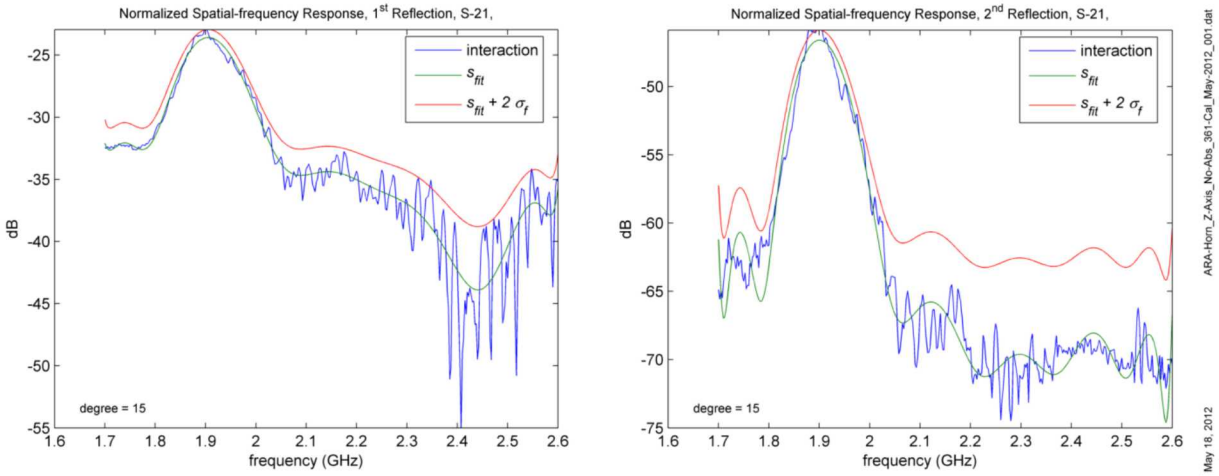

Figure 30 *Normalized spatial-frequency response of the first reflection (left) and second reflection (right), with a 15^{th}-order polynomial curve fit.*

The smooth fits plotted in Figure 30 correspond to n^{th}-degree polynomials with $n = 15$, of the form given in (55). The parameters used in (56) to choose the degree are $n_{max} = 15$, $n_s = 10$, and $n_f = 361$ frequencies. The uncertainty bound for S_{21} due to the reflection between the probe and the antenna is plotted in Figure 31 for this example data set. As to be expected from the removal of absorber, the uncertainty is larger. Notice the significant peak in the uncertainty near 1.9 GHz, where the first-order reflection is much larger than before, and where the second-order reflection is clearly present. However, the second-order reflection is much smaller than the first-order, so the use of only the first-order reflection to compute the uncertainty is justified.

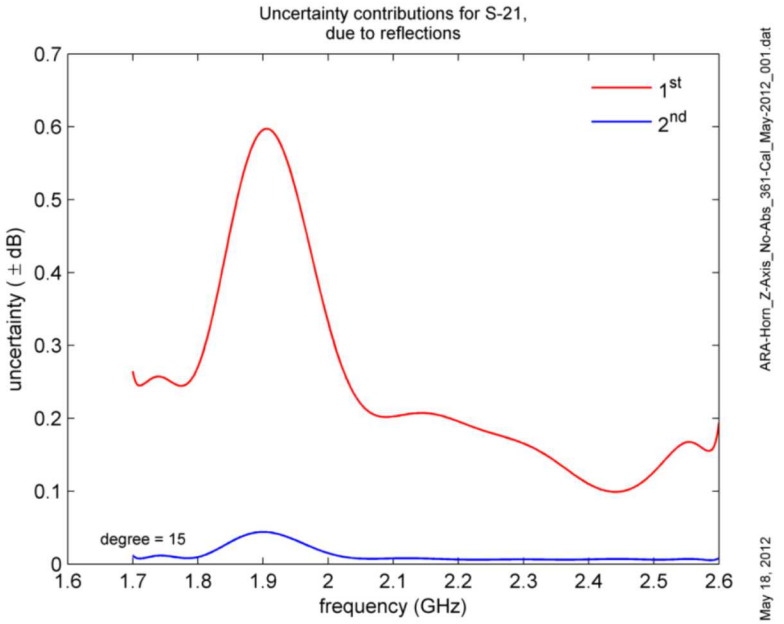

Figure 31 Boresight-gain uncertainty-contribution bounds due to the presence of the first and second reflections.

Measurement showing reflection from a side wall of the chamber

This set of data was acquired with the ARA S-band horn on the large near-field range, but absorber was removed from the floor to demonstrate the spatial-frequency response caused by reflections from a side of the chamber, in this case the floor. The configuration is shown in Figure 32, the floor of which should be compared with the floor in Figure 1. The absence of the absorber on the floor between the horn and the probe will allow a significant reflection to occur that is expected to behave as described by the analytic analysis of a wall reflection.

The magnitude of the measured response is plotted in Figure 33. Ripple consistent with the presence of interfering components is very obvious. Also, for this data set, unlike the previous two sets, the reported Lower Slide position actually increases as the spacing between the probe and antenna increases[9]. The normalized spatial-frequency response is plotted in Figure 34. The absence of the absorber on the floor caused a very strong spatial-frequency response at spatial frequencies below the direct-coupling response. In fact, it appears that there are two reflections from stationary walls. The stronger response occurs at lower spatial frequencies than the weaker response. This implies that the weaker response is either a higher-order response from the floor or is coming from a position somewhat closer than the stronger response, since the analytic model predicts higher spatial frequencies as the reflection point moves closer to the z axis. In comparison, the first reflection between the probe and antenna is producing a much weaker response. The fact that the first-reflection response occurs at lower spatial frequencies than the aperture separation suggests means that these reflections are coming from structure that is offset from the axis, but is moving with either the probe or antenna. This data set also shows the first-reflection response merging into a sidelobe of the direct-coupling response at the low-frequency end of the data set. Collecting data over a larger excursion along the z axis would have reduced the width of the main lobe of the response and also reduced the sidelobe spacing, possibly mitigating this problem. The fact that the first-reflection response is spread over a range of spatial frequencies at each temporal frequency indicates

[9] The FARM utilizes several different model towers, slides, and measurement configurations. The consequence is that the direction of motion for which increasing values are reported by the sensors is not consistent over all configurations. For that reason, the software that performs the spatial-frequency analysis must determine the meaning of the slide position for each data set. Failure to do so correctly will result in negative values for the desired spatial frequencies instead of positive values.

that the first reflection is coming from several parts of the structure that are offset from the range axis, not a single, well-defined point.

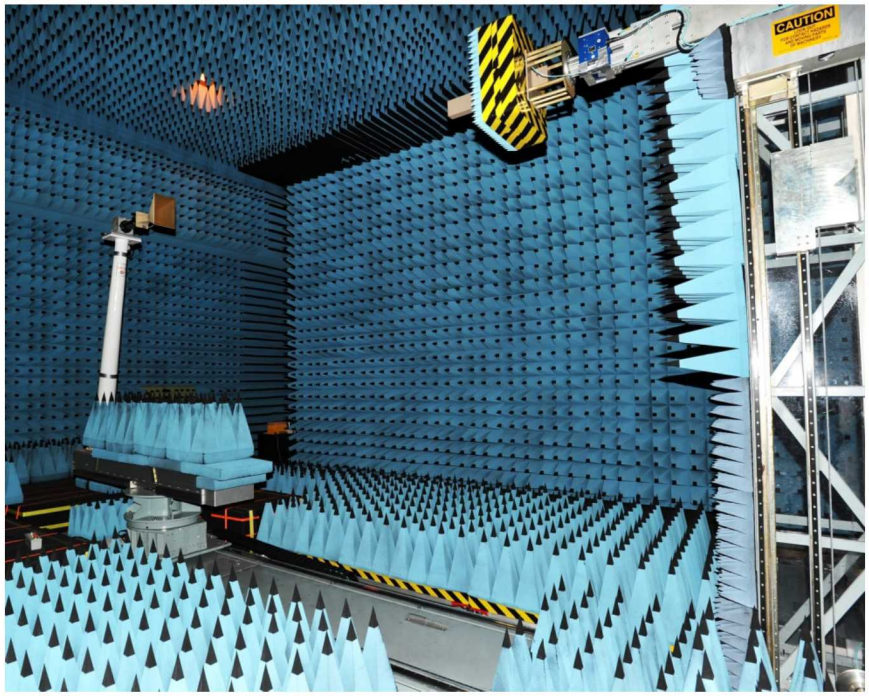

Figure 32 *ARA Horn antenna mounted on the spherical near-field range, with absorber removed from the floor to increase reflection interference.*

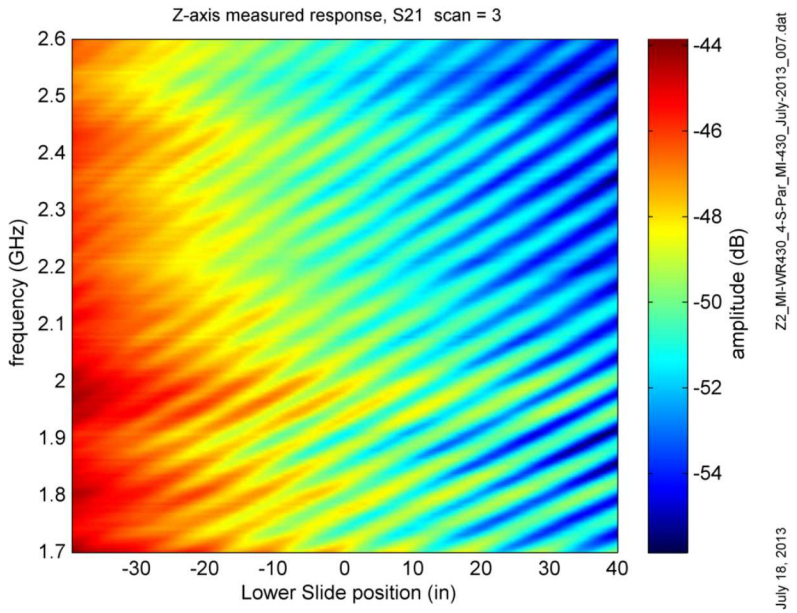

Figure 33 *Magnitude of the measured coupling between the MI-Tech WR-430 open-ended waveguide probe and the ARA S-band horn antenna. The absorber has been removed from the floor between the horn and the probe.*

The peak values of the spatial-frequency response that were extracted by the search algorithm are plotted against the temporal frequency in Figure 35 for the first reflection between the probe and antenna (left) and the exposed floor (right). The data set contains a large number of z-axis samples, so the smooth curves are fit to 15th-degree polynomials. In this case, the response from the floor reflection is entirely dominant over the first-reflection response between the probe and antenna. The resulting contribution to the uncertainty of the boresight gain from each is plotted in Figure 36. The uncertainty contribution from the floor reflection exceeds ±1 dB at some frequencies, underscoring the importance of properly placed absorber in the near-field measurement chamber.

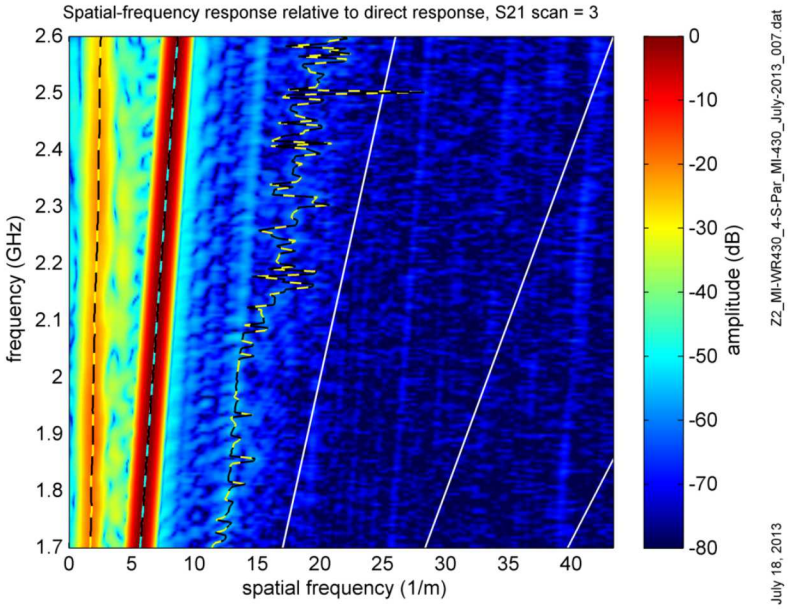

Figure 34 *Normalized spatial-frequency response for the ARA S-band antenna with absorber removed from the floor between the antenna and probe. The presence of a strong reflection is obvious at spatial frequencies below those due to the direct coupling, as predicted by the analytical model.*

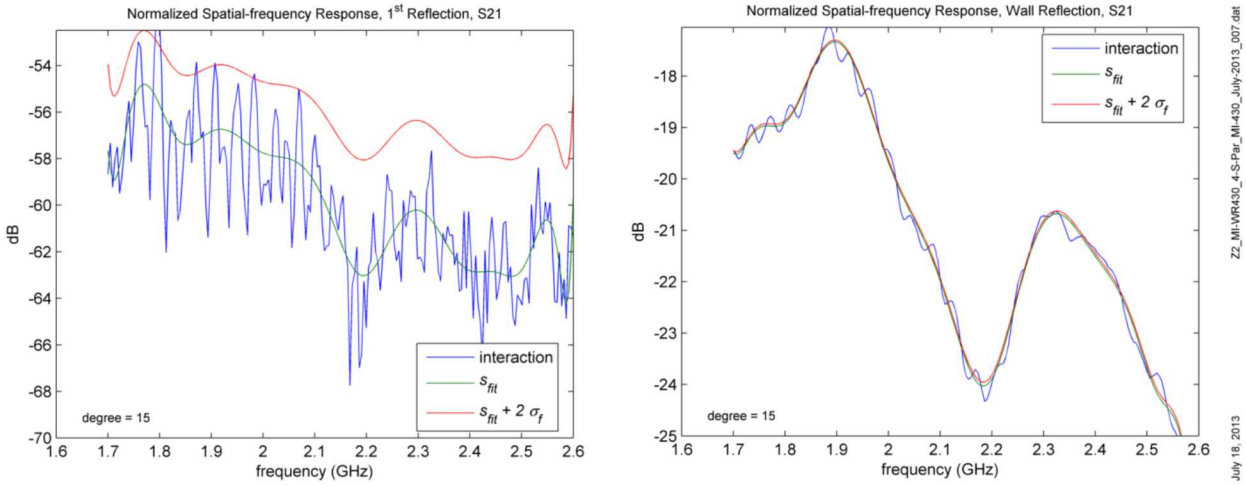

Figure 35 *Spatial-frequency response for the first reflection (left) and the floor (wall) reflection when the absorber has been removed from the floor between the antenna and probe.*

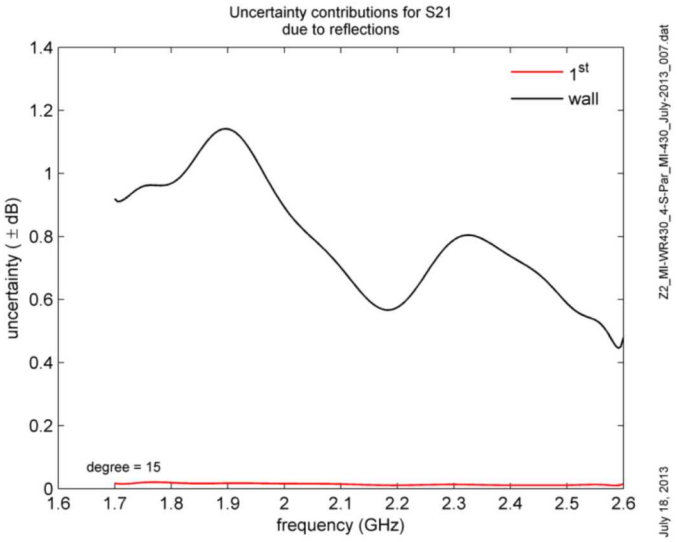

Figure 36 Uncertainty contributions due to the first reflection (red) and the floor reflection (labeled wall) when the absorber has been removed from the floor between the antenna and probe.

Conclusion

A robust method for detecting, identifying, and quantifying reflections that occur on a near-field range has been described, analyzed, and demonstrated. The method is based on the analysis of different spatial frequencies associated both with the direct coupling and with each reflection. These spatial frequencies can be extracted from data obtained as the distance separating the antenna and probe is varied. Unlike time-domain analysis, this spatial-frequency analysis does not require a large bandwidth, and it can even be applied to data collected at a single temporal frequency. This is a significant advantage for antenna measurements, since many antenna designs support only limited or very narrow bandwidths.

The spatial-frequency analysis can identify and distinguish the direct coupling between the probe and the antenna under test, the different order reflections that occur directly between the probe and the antenna, and the reflections that occur from side-walls in the near-field measurement room, including the floor and ceiling. The analytical model shows that the n^{th}-order direct reflection between the probe and antenna produces spatial frequencies near $f_s = \sqrt{2n+1}/\lambda$, where λ is the wavelength, while the spatial frequency associated with the direct coupling is simply $1/\lambda$. The analysis also shows that the dominant reflections from *stationary* structures not centered on the line connecting the antenna and probe are always associated with spatial frequencies smaller than $1/\lambda$. In addition, reflections from objects offset to the side of, but attached to, the antenna or probe are associated with spatial frequencies that are less than those associated with the same order reflection occurring directly between the probe and antenna from on-axis points.

The method involves collecting data in the spatial domain by simply varying the spacing between the antenna under test and the near-field probe. It is recommended that data be obtained with a spacing increment of about $\lambda_{min}/10$, where λ_{min} is the wavelength at the highest frequency to be measured. The range of separation from minimum to maximum should no less than about $N\lambda_{max}$, where λ_{max} is the wavelength of the lowest frequency. A good choice is $N \geq 10$, although values as small as 5 may be useable under some circumstances. It is also recommended that the minimum spacing, z_{min}, should be greater than about $\lambda_{max}/2$.

Measured data obtained on the near-field range at the Sandia Facility for Antenna and Radar-cross-section Measurement has been presented to show the validity and usefulness of the z-axis spatial-frequency analysis. The agreement between the simple analytical model and actual measured data is remarkable, and confirms the validity of this approach. The ease and clarity with which the various interaction components can be detected, separated, identified, and quantified justifies the additional effort required to obtain the z-axis data when performing near-field antenna measurements.

The reflections on the near-field range that have been identified and quantified with this spatial-frequency analysis constitute just some of the contributions to the uncertainty of the measurement of the antenna's gain. Now, having been accurately quantified, these contributions can be combined with other sources of uncertainty to provide a more complete and accurate estimate of the total measurement uncertainty.

As a final thought, consider that the spatial-frequency analysis provides a very good method to filter the direct coupling from various reflections that occur during the near-field measurement, but as applied in the z-axis spatial-frequency analysis, it is used only to quantify a component of the uncertainty in the gain measurement. If the antenna-to-probe separation could be varied quickly enough to allow a suitable number of spherical scans to be completed in a reasonable time, the z-axis spatial-filtering method could be applied to the entire set of spherical near-field data, and the direct coupling could be isolated and extracted intact without reflections. While such a measurement seems impractical with current positioning equipment, it could be of use in an application where minimizing gain uncertainty is critical, such as calibrating a standard-gain horn.

References

[1] J. E. Hansen, ed., *Spherical Near-Field Antenna Measurements*, Peter Peregrinus, Ltd., London, 1988.

[2] T. B. Hansen and A. D. Yaghjian, *Plane-Wave Theory of Time-Domain Fields, Near-Field Scanning Applications*, New York, IEEE Press, 1999.

[3] S. Gregson, J. McCormick, and C. Parini, *Principles of Planar Near-Field Antenna Measurements*, London: Institution of Engineering and Technology, 2007.

[4] Robert E. Collin and Francis J. Zucker, *Antenna Theory Part 1*, McGraw-Hill Book Company, New York, 1969.

[5] David R. Lide, ed., *CRC Handbook of Chemistry and Physics, 89th Edition (Internet Version 2009),* CRC Press, Boca Raton, FL.

[6] I. S. Gradshteyn, I. M Ryzhik, *Table of Integrals, Series, and Products, Corrected and Enlarged Edition*, Academic Press, New York, 1980 (originally published as *Tablitsy Integralov, Summ, Ryadov I Proievedeniy*, Gosudarstvennoe Izdatel'stvo Fiziko-Matematicheskoy Literatury, Moscow, 1963.).

[7] M. Abramowitz and I. A. Stegun, ed., *Handbook of Mathematical Functions with Formulas, Graphs, and Mathematical Tables*, Dover Publications, Inc., New York, 1965, (ninth Dover printing, 1972).

[8] Richard P. Brent and Edwin M. McMillan, "Some New Algorithms for High-Precision Computation of Euler's Constant", *Mathematics of Computation,* Vol., 34, No. 149, January, 1980, pp. 305-312.

[9] Eric W. Weisstein, *CRC Concise Encyclopedia of Mathematics, Second Edition*, CRC Press, Boca Raton, FL, 2002.

[10] Chao-Ping Chen, "Sharpness of Negoi's Inequality for the Euler-Mascheroni Constant", *Bulletin of Mathematical Analysis and Applications,* Vol. 3, Issue 1, 2011, pp 134-141.

[11] Wolfram Research, Inc., *Mathematica*, Version 10, Champaign, IL (2014). Available: http://www.wolfram.com/ .

[12] W. A. Stein *et al.*, *Sage Mathematics Software* (Version 6.5), The Sage Development Team, 2015. Available: http://www.sagemath.org .

[13] Julian Havil, *Gamma: Exploring Euler's Constant*, Princeton University Press, Princeton, 2003.

[14] Jeffrey C. Lagarias, "Euler's Constant: Euler's Work and Modern Developments", *Bulletin (New Series) of the American Mathematical Society*, Volume 50, Number 4, October 2013, Pages 527–628.

Distribution

1	MS 0519	Roger Derek West, 05346
1	MS 0519	Judith A. Ruffner, 05349
1	MS 0519	Armin W. Doerry, 05349
1	MS 0519	Douglas L. Bickel, 05344
1	MS 0519	Ann M. Raynal, 05344
1	MS 0532	Steven Castillo, 05340
1	MS 0532	Bryan L. Burns, 05300
1	MS 0532	William H. Hensley, Jr., 05344
1	MS 0533	Susan Gardner, 05342
1	MS 0533	Robert Riley, 05342
1	MS 0533	Kurt W. Sorensen, 05345
1	MS 0533	Steven E. Allen, 00422
1	MS 0533	Karen Coperich Branch, 05345
1	MS 0533	Billy C. Brock, 05345
1	MS 0533	Dylan A. Crocker, 05345
1	MS 0533	Dale F. Dubbert, 05345
1	MS 0533	Travis W. Eubanks, 05345
1	MS 0533	Gary K. Froehlich, 05345
1	MS 0533	Hung (Jacques) Loui, 05345
1	MS 0533	Jacob J. McDonald, 05345
1	MS 0533	Ward E. Patitz, 05345
1	MS 0533	Bernd H. Strassner II, 05345
1	MS 0533	Matthew W. Young, 05345
1	MS 1217	Nathanael J. Smith, 05964
1	MS 0899	Technical Library, 9536 (electronic copy)


Sandia National Laboratories